A new model for ionospheric total electron content: the impact of solar flux proxies and indices

Larisa P Goncharenko [1], Cole A Tamburri [1,2,3], W Kent Tobiska [4], Samuel J Schonfeld [5], Phillip C Chamberlin [6], Thomas N Woods [6], Leonid Didkovsky [7], Anthea J Coster [1], Shun-Rong Zhang [1]

[1]MIT Haystack Observatory, Westford, MA
[2]University of Colorado, Boulder, CO
[3]Boston College, Chestnut Hill, MA
[4]Space Environment Technologies, Pacific Palisades, CA
[5]Institute for Scientific Research, Boston College, Newton, MA
[6]University of Colorado, Laboratory for Atmospheric and Space Physics, Boulder, CO
[7]Space Sciences Center, University of Southern California

Key Points:

- The study introduces a formulation of new high-resolution empirical model for total electron content
- The impact of several solar flux proxies on the modeling of total electron content is examined
- The FISM2 EUV flux is found to perform the best, closely followed by $S_{10.7}$ index and the Mg II index

Corresponding author: Larisa P. Goncharenko, lpg@mit.edu

Corresponding author: Cole Tamburri, cole.tamburri@colorado.edu

Abstract

We present a new high resolution empirical model for the ionospheric total electron content (TEC). TEC data are obtained from the global navigation satellite system (GNSS) receivers with a 1^o x 1^o spatial resolution and 5 minute temporal resolution. The linear regression model is developed at 45^o N, 0^o E for the years 2000 - 2019 with 30 minute temporal resolution, unprecedented for typical empirical ionospheric models. The model describes dependency of TEC on solar flux, season, geomagnetic activity, and local time. Parameters describing solar and geomagnetic activity are evaluated. In particular, several options for solar flux input to the model are compared, including the traditionally used 10.7cm solar radio flux ($F_{10.7}$), the Mg II core-to-wing ratio, and formulations of the solar extreme ultraviolet flux (EUV). Ultimately, the extreme ultraviolet flux presented by the Flare Irradiance Spectral Model, integrated from 0.05 to 105.05 nm, best represents the solar flux input to the model. TEC time delays to this solar parameter on the order of several days as well as seasonal modulation of the solar flux terms are included. The Ap_3 index and its history are used to reflect the influence of geomagnetic activity. The root mean squared error of the model (relative to the mean TEC observed in the 30-min window) is 1.9539 TECu. A validation of this model for the first three months of 2020 shows excellent agreement with data. The new model shows significant improvement over the International Reference Ionosphere 2016 (IRI-2016) when the two are compared during 2008 and 2012.

1 Introduction

Forecasting the future state of the ionosphere is a fundamental challenge for near-space environment research and operations. In pursuit of this goal, the international space weather community recognizes the need for enhanced fundamental understanding of space weather and its drivers and for improved predictive models of various ionospheric and thermospheric parameters. Recent efforts by the international Community Coordinated Modeling Center have identified several critical ionospheric and thermospheric parameters that can be used for the assessment of the predictive capabilities (Scherliess et al., 2019). These parameters include total electron content (TEC), peak electron density (N_mF_2), and peak electron density height (h_mF_2). Reliable specification and forecasting of these parameters have significant societal impacts, as they can help mitigate uncertainties in precision timing and navigation, which impede space situational awareness, single-band high-frequency radio operations, and satellite geolocation. In particular, TEC is an important parameter for estimation of phase delay effects in the ground-to-satellite navigation signals.

A significant ongoing effort to address these goals includes continuous development of different types of models, including first-principles models of the coupled ionosphere/thermosphere systems, data-assimilative models, and purely empirical models that are based on available observations. Despite significant development and improvement in first-principles models, quantitative validation efforts indicate that empirical models often outperform first-principles models for geomagnetically quiet conditions, though first-principles models can perform better during disturbed conditions if they include more complex and accurate input drivers (Shim et al., 2011, 2012, 2017b, 2018). Amongst the empirical models, the International Reference Ionosphere (IRI) (Bilitza et al., 2017) and NeQuick (Nava et al., 2008) models are best known and most widely used. In particular, the IRI model is the basis for the International Standards Organization (ISO) International Standard IS 16457 (ISO16457, 2014).

Originally developed in the late 1960s, the IRI model has been continuously updated and improved as a result of coordinated dedicated efforts by the international research community. However, it still has certain limitations in simulating TEC. One of them is related to the representation of the electron density profile. The TEC in the IRI

model is obtained through integration of the electron density profile up to 2000 km and thus does not include contributions to TEC from the plasmasphere, which can reach several (2 - 6) TECu (1 TECu = 10^{16} el/m^2) (Yizengaw et al., 2008; Cherniak et al., 2012; Shim et al., 2017a; L. Liu et al., 2018). In addition, the IRI model, as a global model, can significantly overestimate or underestimate regional TEC variations, even for mid-latitude locations (e.g. Zakharenkova et al. (2015)). As the IRI model electron density is based mostly on ionosonde observations below the F-region peak and on observations from Alouetee 1,2 and ISIS 1,2 (Bilitza, 2004) above the F-region peak, deficiency in the description of the topside profile is thought to be the primary reason for the reported differences between IRI and TEC observations (Zakharenkova et al., 2015). The second limitation of IRI is related to its low sensitivity to short-term variations in solar ionizing flux. As the model is aimed at representing monthly mean ionospheric conditions, it uses monthly values of either IG12 (a 12-month running mean of the global ionosphere index) or Rz12 (a 12-month running mean of the sunspot number) which F_{107} can be scaled to.

Recognition of the significant need for more accurate empirical models, together with the continued increase in availability and quality of ionospheric data, has led to a rapid development in additional empirical models during the last several years. Expansion of TEC data obtained from the GNSS satellites presented an opportunity to develop independent TEC models that do not rely on vertical extrapolation of the electron density profile or assumptions about the shape of the profile above the peak electron density, like in IRI or NeQuick. Such TEC models can be broadly characterized as global, regional, or local. Several global models were developed based on Global Ionospheric Maps (GIMs) which are generated since 1998 with 2-hour temporal resolution (Mannucci et al., 1998; Vergados et al., 2016; Komjathy et al., 2005). Mukhtarov et al. (2013a) has built a monthly mean TEC model with 5^o x 5^o degree resolution in latitude and longitude utilizing data from the Center for Orbit Determination of Europe (CODE) and representing TEC variations as a function of solar flux, rate of change in solar flux, season, time of day, and magnetic latitude; further development of that model included dependence on geomagnetic activity (Mukhtarov et al., 2013b). Aa et al. (2012) developed a global TEC model based on GIMs provided by the Jet Propulsion Laboratory (JPL) and using empirical orthogonal function (EOF) analysis, a technique which decomposes data using functions determined by the data themselves rather than the predefined functions used in other methods such as Fourier decomposition (Chen et al., 2015). Lean et al. (2016) constructed a model of 2-hourly TEC data by combining representations of solar EUV, sinusoidal parameterizations of annual, semiannual, terannual, and biennial oscillations, diurnal, semidiurnal, and terdiurnal cycles, and geomagnetic activity. The distinctive feature of the Lean et al. (2016) model is the description of solar ionizing flux; it includes total EUV irradiance summarized for wavelengths less than 105 nm and 11 time lags ranging from 0 and 12 hours to 36 days. Recognizing the limitations of IGS TEC GIM maps and their lower accuracy over the oceans, Feng et al. (2019) suggested a global TERMGRID model that consists of 5183 independent single point empirical models.

Many new TEC empirical models were developed for the description of the regional ionosphere, including, for example, the ionosphere over Europe (Jakowski et al., 2011), China (Mao et al., 2008), North America (Chen et al., 2015), South Africa (Habarulema et al., 2010, 2011), Australia (Bouya et al., 2010), and the Arctic (J. Liu et al., 2014). Regional empirical models often outperform global empirical models as they are based on additional data not included in IGS GIM maps and use fewer assumptions about spatial variations in TEC. Single-location empirical models are often used to describe distinctive ionospheric features over a specific geographic location and/or explore different modeling approaches (Mao et al., 2005; J. Liu et al., 2012; Huang & Yuan, 2014). Empirical ionospheric modeling remains an active area of research, as increasingly accurate and detailed global specification of the near-Earth space environment is required to further understand its intricate organization and behavior.

Ionospheric electron density is produced by solar EUV radiation at wavelengths less than 103 nm (Schunk and Nagy, 2009) that ionizes thermospheric atomic oxygen and molecular nitrogen and oxygen. The most important contribution to ionization comes from EUV radiation at wavelengths 26-34 nm which is mostly absorbed by atomic oxygen at altitudes above 200 km (Richards et al., 1994; Schunk & Nagy, 2009). Solar EUV flux is also an important source of atmospheric heating, determining neutral temperature, composition and winds which are all directly coupled to the ionospheric photo-ionization, chemistry, and dynamics. Previous studies have demonstrated that solar EUV emission can be well described by the solar activity proxy $F_{10.7}$ which represents solar radio flux at the wavelength of 10.7 cm. We use the definitions of solar index and solar proxy from IS 21348 where a solar proxy is a data type used as a substitute for solar spectral irradiances at other wavelengths or bandpasses and a solar index is a data type that is an activity level indicator. The vast majority of empirical ionospheric models, even those developed most recently, use the $F_{10.7}$ proxy to describe solar EUV influence on ionospheric parameters (Mukhtarov et al., 2013a, 2013b; Chen et al., 2015; Themens et al., 2017; Feng et al., 2019; Zhang et al., 2005). The popularity of the $F_{10.7}$ proxy is based on its long data record, as it is available since 1947, and well-demonstrated performance for the description of critical frequency f_oF_2 (or peak electron density N_mF_2) that was historically widely available due to the abundance of ionosondes (L. Liu et al., 2006). However, the $F_{10.7}$ proxy does not directly describe the solar emission in the EUV wavelength range < 102.5 nm which is directly responsible for the ionization of the thermosphere. In addition, as a significant portion of the contribution to TEC comes from the profile of electron density above the peak, and the impact of different portions of the EUV spectrum varies with altitude, it is not immediately clear if the $F_{10.7}$ proxy performs as well for TEC as for f_oF_2. With increasing availability of satellite EUV data, numerous observational datasets and new indices became available within the last two decades that can better characterize solar energy input to the thermosphere. These observations include solar extreme ultraviolet monitor (SEM) onboard the Solar and Heliospheric Observatory (SOHO), Solar Backscatter Ultraviolet (SBUV) spectrometer on NOAA satellites (Viereck et al., 2001), and SEE onboard TIMED (T. Woods et al., 2000; T. N. Woods, 2005). New indices include, for example, the $S_{10.7}$ index that reflects integrated solar emission between 26 - 34 nm (W. K. Tobiska et al., 2008; B. Bowman et al., 2008a), the Mg II core-to-wing ratio that corresponds to emission near 160 nm (Viereck et al., 2001; B. Bowman et al., 2008a), the $M_{10.7}$ index which is derived from the Mg II (W. K. Tobiska et al., 2008; B. Bowman et al., 2008a), the X_{b10} index that corresponds to 0.1–0.8 nm solar X-ray emission (W. Tobiska & Bouwer, 2005), and the $Y_{10.7}$ index that combines X_{b10} and Lyman-alpha emission. The impact of these indices is better studied in the thermosphere, and their usage substantially improved thermospheric density models (W. K. Tobiska et al., 2008; B. Bowman et al., 2008a; Emmert et al., 2008; He et al., 2018). However, the impact of these indices on improvement in ionospheric empirical models and, specifically, on TEC, is much less known. Maruyama (2010) compared the performance of models that include the sunspot number R, solar $F_{10.7}$ proxy, Mg II index or $S_{10.7}$ index on mid-latitude TEC over Japan and concluded that the $S_{10.7}$ index was the best proxy for modeling TEC of those included in the study. Lean et al. (2011) used TIMED SEE observations with the $F_{10.7}$ proxy and the Mg II index to develop a model of EUV variability and later use it in the global TEC model (Lean et al., 2016; Lean, 2019). It is thus of great interest to further examine whether new solar flux indices are better suited for empirical models of TEC than the $F_{10.7}$ proxy.

Another issue with the $F_{10.7}$ proxy relates to its ability to describe both the direct impact on ionospheric electron density (through ionization processes) and indirect impact (through thermospheric heating that operates on longer temporal scales). The response of electron density to an increase in $F_{10.7}$ saturates for high levels of solar activity, usually between 160 and 200 sfu (1 sfu = $10^{-22}Wm^{-2}Hz^{-1}$), depending on latitude (Lei et al., 2005; L. Liu et al., 2006). To account for this saturation, various ionospheric models usually use a combination of the $F_{10.7}$ flux and the 81-day average of $F_{10.7}$ flux

(Richards et al., 1994; L. Liu et al., 2006; Brum et al., 2011). While it might be sufficient for some types of studies, the need to rely on the knowledge of solar flux that will occur up to 40 days in the future is not acceptable for ionospheric predictions. Maruyama (2010) investigated the delayed response of TEC to several solar flux proxies and concluded that inclusion of 1-2 day delays, the 27-day delay, and the 81-day delay improved TEC modeling. The 2-day delay in the neutral atmosphere, especially in the temperature (Zhang et al., 2015), is a very pronounced feature that has been well recognized and included in the MSIS models. Lean et al. (2016) found that adding several lagged terms with 1-36 day delays of daily solar EUV irradiance alleviates the need for 81-day averaging of solar flux. Thus, the concept of using delayed solar flux terms instead of the 81-day average term has been already introduced and demonstrated.

This paper describes a first phase in a new empirical TEC model that has several distinct features as compared to already available models. It uses TEC data from the CEDAR Madrigal database that are obtained with much higher resolution in space and time as compared to GIM TEC. Recognizing that representation of diurnal behavior with superposition of harmonics with a 24-hr period, 12-hr period, etc., results in an inadequate description of diurnal behavior, especially around sunrise and sunset, the proposed model is based on independent fitting of TEC with 30-min temporal resolution. As a main portion of the current effort, we examine different representations of the solar ionizing flux in order to determine the solar flux proxy most suitable for TEC. In addition, the model considers the delayed response of TEC to solar ionization. In this study, the proposed model and solar flux proxies are examined for a single mid-latitude location, 45°N and 0°E. Future efforts will present extension of this approach to other locations.

2 Data Sources and Preparation

2.1 CEDAR Madrigal Database

In this new empirical model, we use the CEDAR Madrigal database for TEC observations that were processed, and provided for public access, by the Massachusetts Institute of Technology's Haystack Observatory (Rideout & Coster, 2006; Vierinen et al., 2016). This database includes ionospheric observations from an ever increasing set of globally distributed GNSS dual-frequency ground-based receivers, beginning with 500 receivers in 2000 to more than 6000 in 2020. By including data from all publicly available multi-frequency GNSS receivers, and by providing data products at a high cadence (5 min) and high spatial resolution (1 deg latitude and longitude), the Madrigal standard vertical TEC product provides a more comprehensive and detailed description of TEC variations than the GIM TEC product. GIM TEC products are based on only the several hundred IGS receivers, and are available at a 2 hour cadence in a bin of 5 degrees latitude and longitude. The procedure used in the Madrigal processing to calculate the unknown satellite and receiver biases is provided in Vierinen et al. (2016). Although not used here, a new higher resolution TEC product is also available in Madrigal that includes all of the line-of-sight TEC at 1 min resolution. The standard Madrigal TEC product is available in the CEDAR Madrigal database from January 1, 2000. The empirical model discussed in this study is based on 20 years of TEC data, from January 1, 2000 to December 31, 2019, almost two solar cycles of data. This large dataset is well suited for empirical modeling, as it provides good coverage of both solar minimum and solar maximum conditions, and contains a large number of geomagnetic storms.

2.2 Data Preparation and Error Reduction

Techniques for error and noise reduction in these data are employed nevertheless. The data are of varying quality, with clear outliers present at times. For example, from -33° longitude to -27° longitude, data is scarce. In addition to the incongruous completeness of the data set, small artificial variations in TEC track the motion of satellites ac-

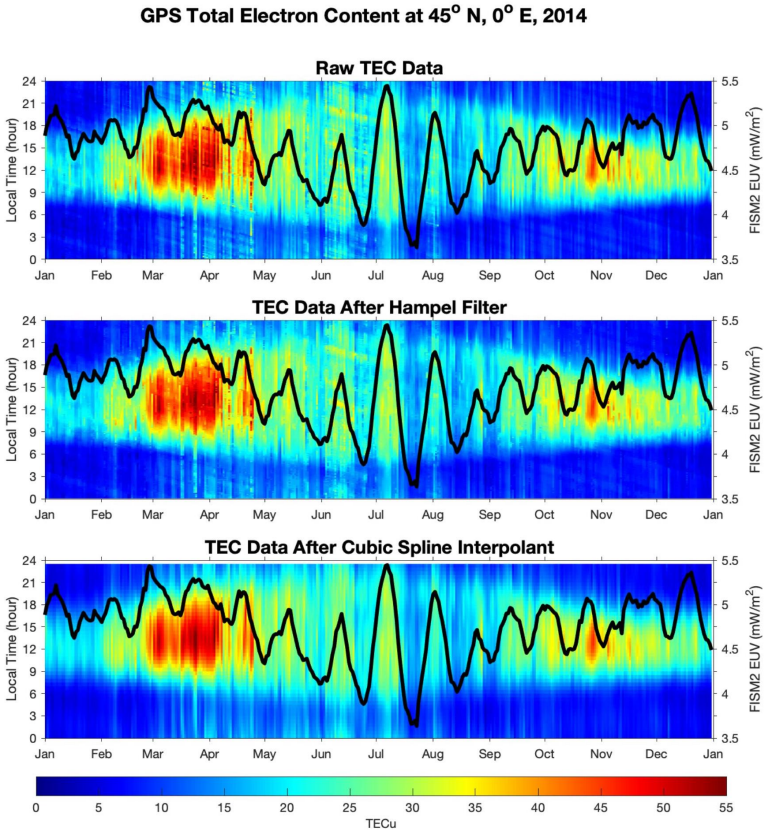

Figure 1. An example of the data cleaning process for the year 2014 at 45°N, 0°E. The solar flux proxy used in the model is shown as a black line to indicate the correlation between increases in solar flux and TEC. Periodic fluctuations in TEC and solar flux also occur in concert.

cording to sidereal hour rather than universal time (UT) hour. These variations are roughly the same magnitude as small-scale fluctuations in TEC which the model ideally reflects. It is therefore important to minimize or remove the error due to this sidereal motion prior to model construction.

To account for the first issue in data quality (the presence of outliers), a Hampel filter is applied with a 13-point window and a 1-standard-deviation criterion for outlier detection. If a given point varies from the median of 13 surrounding data points by 1 standard deviation, the datum is replaced with the median of the 13-point window. A similar filter is then applied, ordering the data from day-to-day rather than hour-to-hour, with a 3-day window around each point and a 3-standard-deviation criterion for outlier replacement. After the application of this filter, in order to account for the sidereal motion of satellites, a cubic spline interpolant is applied to the data with a low tolerance for outlier removal. Figure 1 shows the result of this process for the year 2014 at 45^oN, 0^oE.

2.3 Solar Flux Proxies

One of the goals of this study is to compare the impact of different solar flux formulations on the performance of the new empirical TEC model. We examined 11 solar flux formulations that include direct EUV measurements, proxies that are measured directly ($F_{10.7}$, Mg II core-to-wing ratio, Lyman-alpha), proxies that are special cases of measurements ($S_{10.7}$, corrected $F_{10.7}$, $P_{10.7}$) and finally the proxies from solar irradiance models (SIP $E_{10.7}$, FISM2 EUV). This section presents several recently developed proxies that were not yet applied to an ionospheric model and compares them to proxies traditionally used in studying the solar influence on the upper atmosphere. The utilized solar flux data over the course of 2000 - 2019 (time period used in model development) are shown in Figure 2.

2.3.1 TIMED SEE EUV

The Thermosphere Ionosphere Mesosphere Energetics Dynamics (TIMED) spacecraft includes the Solar EUV Experiment (SEE) as one of its four scientific instruments (T. N. Woods, 2005). The data is available from the University of Colorado at Boulder Laboratory for Atmospheric and Space Physics (LASP) website (`http://lasp.colorado.edu/home/see/data/`), and an overview of the data for 2000 - 2019 is shown in Figure 2(a). Flux measurements are provided for each nanometer in the EUV range; for this study, the data were processed by integrating from 0.5 to 105 nanometers. There are noteworthy omissions in the TIMED SEE EUV data which prompt evaluation of other datasets describing variation in the EUV range. These include (i) that the TIMED mission was launched in 2002, two years after the commencement of the TEC data collected by the Madrigal database, and (ii) that there exist several data gaps, typically associated with the TIMED "safe mode," within the 2002-2019 tenure of the data. These result in a significant lack of data around the maximum of solar cycle 23.

2.3.2 SOHO SEM EUV

The Solar and Heliospheric Observatory (SOHO) spacecraft includes the Solar EUV Monitor (SEM), the data for which are made available by USC Dornsife (`https://dornsifecms.usc.edu/space-sciences-center/download-sem-data/`) and are shown for the relevant time period in Figure 2(b). These data provide the 0.1 - 50 nanometer flux as a daily average value, normalized to 1 astronomical unit (AU). Although a smaller wavelength range than the TIMED SEE data, it includes the 26 - 34 nanometer bandwidth which is considered the primary driver of ionization in the F-region ionosphere. Therefore, this dataset is considered valuable despite its omission of radiation in the 50 - 105 nanometer range included in other EUV data. The data are available with a 15 second

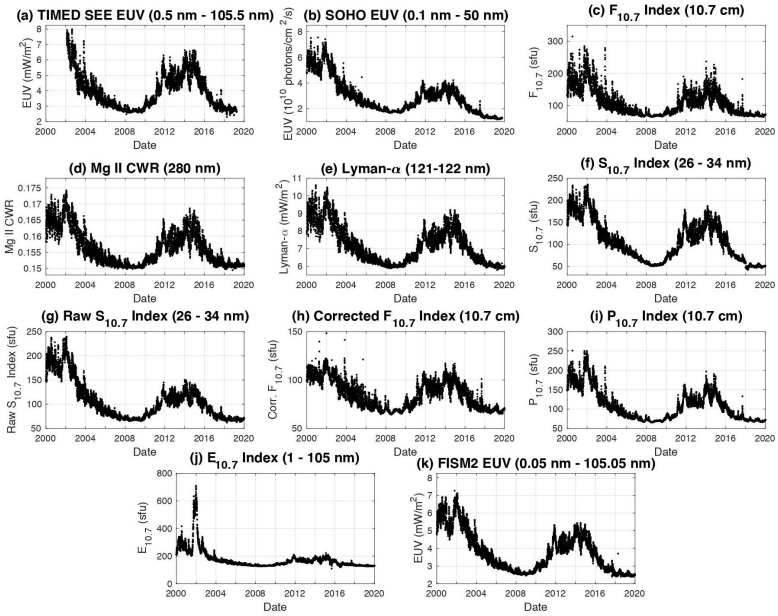

Figure 2. Time series comparison of the solar flux proxies studied for the period over which the model is built. Only the TIMED SEE EUV data do not cover the entirety of the 2000 to 2019 period, having commenced in 2002.

cadence for 2018 and 2019 and a daily average for 1996 through 2019. The latter are used for the present modeling purposes.

2.3.3 $F_{10.7}$

Past empirical models for ionospheric TEC have typically used the 10.7 centimeter radio flux density ($F_{10.7}$) as the input proxy for solar flux. This is partially due to the temporal coverage provided by the $F_{10.7}$ dataset. Developed first in 1947, this proxy provides a data source for solar variability across several solar cycles. It is mostly the extreme ultraviolet (EUV) wavelengths - roughly the 26 to 34 nanometer bandwidth in particular - which directly ionize the F-region ionosphere and are therefore absorbed before reaching the ground. While it does not directly contribute to ionization or atmospheric heating, $F_{10.7}$ has been shown to correlate with satellite acceleration (Jacchia, 1959) and EUV variability over multi-year time scales (Lean et al., 2011).

Data for $F_{10.7}$ are available for more than six solar cycles. The data used here are provided by the CEDAR Madrigal database and shown in Figure 2(c). It should be noted that $F_{10.7}$ is a daily value measured between 17-20 UT. In ionospheric TEC models, the index is typically applied in conjunction with an 81-day moving average, which takes the mean of $F_{10.7}$ values 40 days prior to and following the day in question (F_{81}). The International Reference Ionosphere (IRI) model depends on sunspot number (Rz12) and an ionosphere-effective solar index (IG12), and includes both the daily $F_{10.7}$ and F_{81} as solar flux and ionospheric inputs. Feng et al. (2019) use an average of these two indices as their solar flux input parameter. Mukhtarov et al. (2013b) use the daily $F_{10.7}$ and the linear rate of change of $F_{10.7}$, K_F.

2.3.4 Mg II Core-to-Wing ratio

The Mg II index is the core-to-wing ratio of the Mg II Fraunhofer doublet centered at 280 nanometers (Heath & Schlesinger, 1986). The k and h emission lines at 279.55 and 280.27 nanometers are generated in the upper chromosphere, with nearby wings ("background") generated in the upper photosphere. Calculation of the ratio between these emission lines and nearby wings provides a measure for chromospheric activity which is often used as a proxy for the extreme ultraviolet flux. The data, the relevant subset of which are shown in Figure 2(d), are available since 1978 and are developed as a composite index from several data sources (`http://www.iup.uni-bremen.de/UVSAT/Datasets/mgii`), including the Global Ozone Monitoring Experiment (GOME), Scanning Imaging Absorption Spectrometer for Atmospheric Chartography (SCIAMACHY), GOME-2A, GOME-2B, and GOME-2C missions. These data are updated daily. Viereck et al. (2001) suggested for the period of 1978 through 2000 that the Mg II core-to-wing ratio serves as a better proxy for EUV radiation in the region of most concern to the ionosphere (roughly 26 to 34 nanometer wavelengths) than the $F_{10.7}$ index. Its performance in representing the radiation corresponding to this wavelength range makes it particularly applicable to the study at hand.

2.3.5 Lyman-Alpha Index

Machol et al. (2019) describes the development of the Lyman-alpha (Lyman-α) composite. This represents the solar output at 121.56 nm, the strongest solar vacuum ultraviolet emission line. The data are available from the LASP Interactive Solar Irradiance Data Center (`http://lasp.colorado.edu/lisird/`), and the corresponding time series for 2000 - 2019 is shown in Figure 2(e). The time series takes into account measurements from several instruments and models, as listed on the LASP Interactive Solar Irradiance Data Center webpage corresponding to the dataset. Machol et al. (2019) describe the scaling of the values from each dataset to match the SORCE SOLSTICE reference levels at 1 astronomical unit (AU).

2.3.6 Jacchia-Bowman 2008 (JB2008) $S_{10.7}$ index

W. K. Tobiska et al. (2008) and ISO14222 (2013) describe the development of the $S_{10.7}$ index, a solar flux proxy measured by the SOHO Solar Extreme-ultraviolet Monitor (SEM), the TIMED SEE, the SDO EVE, the GOES-14,-15 EUVS, and the GOES-16,-17 EXIS. It isolates the 26 - 34 nanometer range, the bandwidth which has the most physical impact on ionization in the F-region ionosphere (Banks & Kockarts, 1973). The daily values are available for download at the Jacchia-Bowman 2008 Empirical Thermospheric Density Model (JB2008) website (`https://sol.spacenvironment.net/JB2008/`). The 2000 - 2019 time series is shown in Figure 2(f). The data are available since 16 December 1995 and are updated daily. The relationship between the $F_{10.7}$ and $S_{10.7}$ indices is shown in the middle panel of Figure 3. The best-fitting function between the two indices is quartic after scaling $S_{10.7}$ to the units of $F_{10.7}$. It is notable that the relationship between the two is not linear, though directly proportional.

In addition to the $S_{10.7}$ index, which is modified to remove energy at the top of the atmosphere during solar minimum as a method of compensating for thermospheric cooling at the bottom of the thermosphere, a pure solar version of this index, also called raw without the energy removal, is tested. The corresponding time series is shown in Figure 2(g). It is found that the official $S_{10.7}$ index, described above, yields a better-performing ionospheric TEC model. These results are discussed below.

2.3.7 *Corrected* $F_{10.7}$

Seeking to correct for some discrepancy observed between $F_{10.7}$ and EUV, Schonfeld et al. (2019) present a corrected $F_{10.7}$ index by decomposing $F_{10.7}$ into radiation produced by optically thick bremsstrahlung radiation, optically thin bresstrahlung radiation, and optically thick gyroresonence radiation. These components correspond to radiation from the chromosphere, transition region and corona, and the cores of active regions in the corona, respectively. It is the optically thin bremsstrahlung radiation (corrected $F_{10.7}$ proxy), the data for which are shown in Figure 2(h), which is suggested for use in place of $F_{10.7}$ to approximate solar EUV output. A fit between the traditional $F_{10.7}$ and the corrected $F_{10.7}$ shows a linear relationship up to about $F_{10.7}$ equal to 96 solar flux units (sfu) and a power law for solar flux values above 96 sfu. The top panel of Figure 3 shows this relationship, reproduced from the fit derived in Schonfeld et al. (2019). The spread in the data around the piecewise fit is due to the conversion between the observed $F_{10.7}$ and the 1 AU-adjusted $F_{10.7}$ on which these fits are defined. Converting $F_{10.7}$ to its 1 AU-equivalent, applying the correction, and then reversing the 1 AU-conversion yields the tight spread, with the sharp upper and lower limits resulting from the maximum and minimum Earth-Sun separations, respectively. This index is available for the entire duration of $F_{10.7}$.

2.3.8 $P_{10.7}$ *Index*

Also derived from $F_{10.7}$ is the $P_{10.7}$ index, calculated by taking the mean of the real-time $F_{10.7}$ with the 81-day averaged $F_{10.7}$ index (F_{81}). This index is used in other ionospheric models to capture solar variability, as described above, but presents a philosophical dilemma by using future values of solar flux to predict TEC (Lean et al., 2016). Equation (1) shows the method used to calculate the values corresponding to this input parameter. Figure 2(i) shows the time series corresponding to this index.

$$P_{10.7} = (F_{10.7} + F_{81})/2 \tag{1}$$

2.3.9 *Solar Irradiance Platform (SIP)* $E_{10.7}$

The Solar Irradiance Platform (SIP, formerly the SOLAR2000 model), provides a comprehensive solar spectrum developed by the Space Environment Technologies (SET) company (`http://www.spacewx.com/solar2000.html`). The company has developed several proxies for solar activity and provides them to the research community. The $E_{10.7}$ index, shown in Figure 2(j), most closely resembles the solar EUV spectrum by reporting the flux from 1 - 105 nanometers scaled to solar flux units (sfu). The index reflects general solar activity on 27-day and solar cycle (11 year) time scales (W. K. Tobiska, 2002). The index was developed with the intention of capturing the solar cycle variability and output most directly influential on the ionosphere-thermosphere system. However, as shown in Figure 2(f), the index shows a sharp peak in late 2001 and early 2002 not reflected in the other EUV datasets. This is found to have a detrimental effect on the model as discussed below.

2.3.10 *Flare Irradiance Spectral Model EUV*

The Flare Irradiance Spectral Model (FISM) is an empirical model which estimates the solar irradiance in the EUV range with a time cadence of one day and a spectral resolution of 0.1 nm, ten times better resolved than TIMED SEE EUV. FISM was developed to improve the accuracy of space weather model estimations (Chamberlin et al., 2007). In addition, the development of this model increases temporal resolution for the sake of capturing variations due to solar flares (Chamberlin et al., 2008). Here we use version 2 of the FISM data. The proxy is available in bands from 0 to 190 nanometers,

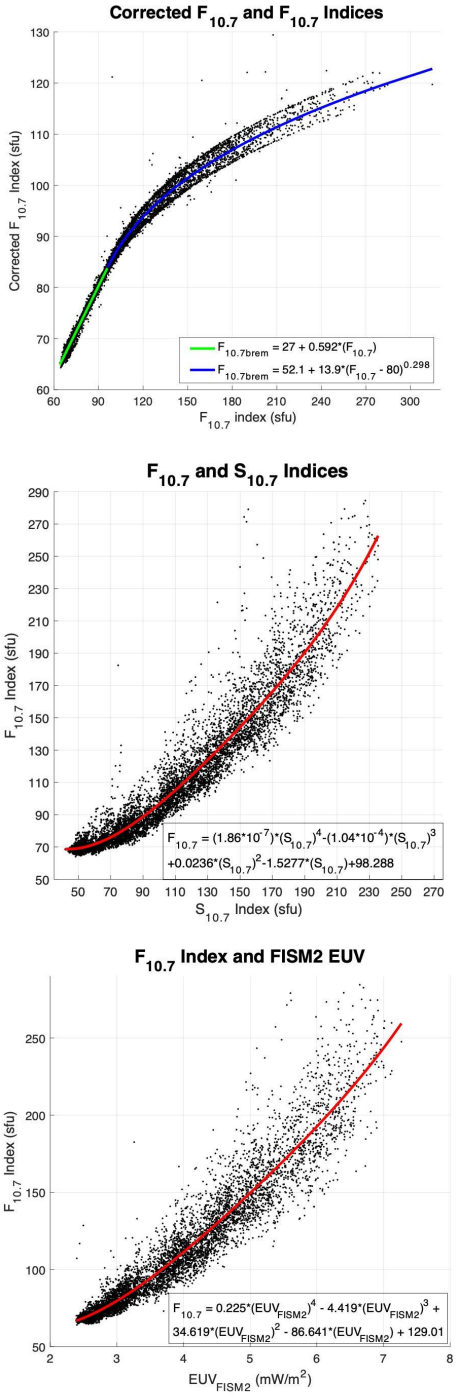

Figure 3. Verification of the fit between the corrected $F_{10.7}$ proxy and the original $F_{10.7}$, as provided in Schonfeld et al. (2019) (top). Relationship between $F_{10.7}$ and $S_{10.7}$ for the years 2000 through 2019 (middle). Relationship between $F_{10.7}$ and FISM2 EUV for the years 2000 through 2019 (bottom).

although, as with the TIMED SEE data, only the 0.05 to 105.05 nanometer wavelength bins are used here. The data were processed by integrating across this bandpass. Upon investigation it was found that the inclusion of higher wavelengths in the EUV range does not significantly contribute to the performance of the ionospheric model. The data are available from the LASP Interactive Solar Irradiance Data Center (`http://lasp.colorado.edu/lisird/`), and are shown for the 2000 - 2019 period in Figure 2(k). The relationship between the $F_{10.7}$ and FISM2 indices is shown in the bottom panel of Figure 3.

3 Formulation of the New Empirical Model

We construct a model of TEC variation at a given location (45^{o}N, 0^{o}E in this specific case) as a function of solar flux, season, and geomagnetic activity through a multiple linear regression fit of the observed TEC to time series of solar flux proxies (with multiple delays), seasonal oscillations, geomagnetic activity indices (with multiple delays), and cross-modulation of these terms. Explicitly, the model is formulated as follows:

$$TEC(t, DOY) = TEC_0 + TEC_{sol}(t) + TEC_{seas}(DOY) + TEC_{geo}(t) + TEC_{cr-terms}(t, DOY), \tag{2}$$

where

$$TEC_{sol}(t) = \sum_{n=0}^{n_{sol}} a_n F(t-n) + bF^2(t); n = 0,\ 1,\ 8,\ 24,\ 36\, days \tag{3}$$

$$TEC_{seas}(DOY) = \sum_{m=1}^{m_{seas}} c_m \sin\left(\frac{2\pi DOY m}{365}\right) + d_m \cos\left(\frac{2\pi DOY m}{365}\right); m = 1,\ 2,\ 3,\ 4 \tag{4}$$

$$TEC_{geo}(t) = \sum_{l=0}^{l_{geo}} e_l Ap_3(t-l) + \sum_{l_1=0}^{l_{1,geo}} e_{l1} Ap_3(t-l_1); l = 0,\ 3,\ 24,\ 48,\ 72\, hours; l_1 = 0,\ 48\, hours \tag{5}$$

$$\begin{aligned} TEC_{cr-terms}(t, DOY) = & \\ & \sum_{k_1=1}^{3} f_{k_1} F(t) \sin\left(\frac{2\pi DOY k_1}{365}\right) + g_{k_1} F(t) \cos\left(\frac{2\pi DOY k_1}{365}\right) \\ & + \sum_{k_2=1}^{4} f_{k_2} F(t)^2 \sin\left(\frac{2\pi DOY k_2}{365}\right) + g_{k_2} F(t)^2 \cos\left(\frac{2\pi DOY k_2}{365}\right) \end{aligned} \tag{6}$$

Equation (3) describes the TEC response to solar activity, where F is a solar activity proxy (i.e. one of the proxies described in section 2.3) and n is a temporal lag of this proxy (in days). As formulation of the model allows easy manipulation with addition or exclusion of different terms, extensive testing of different lags in the solar activity proxy was performed. Delay terms of 1 day, 2 days, 3 days, 4 days, 6 days, 8 days, 24 days, and 36 days were considered for the solar flux terms in addition to the real-time (0 hour delay) term. Although delay terms with 2-6 days showed some statistical significance, their inclusion resulted in lower coefficients for real-time solar flux terms, but did not lead to meaningful improvement of the model. Ultimately, only the real-time, 1-day delay, 8-day delay, 24-day delay, and 36-day delay terms showed highest significance, and the n listed after the formula indicates solar proxy delays that were included

in the current version of the model (n = 0, 1, 8, 24, 36 days). Note that a square term for the real-time solar proxy is also included. Equation (4) describes seasonal variation as a combination of sine and cosine functions that correspond to annual, semi-annual, 4-month, and 3-month variations. Shorter-term variations (4-months, 3-months) were found to be significant and improve the description of the timing for equinoctial enhancements in TEC. Equation (5) describes the dependence on geomagnetic activity as a function of Ap_3 index and different temporal lags of Ap_3 index. Several temporal Ap_3 lags were included in the model after extensive testing for their statistical significance, specifically, 3-hr, 24-hr, 48-hr, and 72-hr. Finally, equation (6) describes the statistically significant cross-terms (e.g. amplitude modulation of solar flux and seasonal terms). This approach produces 35 fitting coefficients a, b, c, d, e, and f. We note that solar flux terms and geomagnetic activity terms were standardized based on the median and standard deviation of the observed values in the 20-year period considered in this study.

The standardization technique is shown in equations (7) - (10), where F_{med} and $Ap_{3\,med}$ are the medians of the FISM2 EUV and Ap_3 index, respectively, calculated for each LT, and F_{std} and $Ap_{3\,std}$ are the standard deviations of the FISM2 and Ap_3 indices, respectively, calculated for each LT. Squared variables are not standardized independently, but rather are calculated by squaring the standardized linear terms. This is done to reduce multicollinearity without affecting the correlation coefficients with other variables (Kim & Dong-Ku, 2011). We slightly modify this method by using the median rather than the mean to account for the large number of statistical outliers which exist in both the solar flux and geomagnetic datasets.

$$EUV_{FISM2}(t-n)_{\,stand} = [EUV_{FISM2}(t-n) - F_{med}]/(F_{std});\ n = 0,\ 1,\ 8,\ 24,\ 36\,days \quad (7)$$

$$EUV_{FISM2}{}^{2}_{stand} = (EUV_{FISM2\,stand})^2 \quad (8)$$

$$Ap_3(t-l)_{\,stand} = [Ap_3(t-l) - Ap_{3\,med}]/(Ap_{3\,std});\ l = 0,\ 3,\ 24,\ 48,\ 72\,hours \quad (9)$$

$$Ap_3{}^{2}(t-l_1)_{\,stand} = [Ap_3(t-l_1)_{\,stand}]^2;\ l_1 = 0,\ 48\,hours \quad (10)$$

A distinctive feature of this model is its description of diurnal behavior. While most other models describe diurnal behavior as a superposition of sines and cosines with 24-hr, 12-hr, and 8-hr periods, this model is composed of 48 separate models, i.e. every 30-min bin of TEC is fitted with equations (2) - (6), resulting in 1680 fitting coefficients for a local model. This approach is similar to that used by Themens et al. (2017) and allows accurate description of diurnal behavior, especially the rapid TEC increase after the sunrise and decrease after the sunset. This formulation is also useful in assessing the importance of each predictor at different local times. To construct the model, we have used 90% of the available TEC data, randomly selected out of all 20 years of observations. The remaining 10% of data were used for testing purposes. Statistical significance of each input parameter in equations (2) - (6) was examined based on ANOVA tables and P values. While not all UT time bins had high statistical significance for all predictors, all showed significance at some point during the day, and therefore were included in the model. For example, the squared 48-hour delayed Ap_3 index (Equation 5) was relatively insignificant from 0-4UT and 8-17UT, but highly significant (P value less than 0.01) from 5-7UT and 19-24UT. Section 5.1 discusses this aspect in more detail.

Data inspection showed that in addition to data quality issues on the scale of a few days, long-term errors (e.g. artificially elevated readings for TEC lasting more than a

	RMSE (TECu)	MSE ($TECu^2$)	MAE (TECu)	MAPE (%)	Correlation Coefficient	Mean of Data-Model Difference (TECu)
SOHO EUV	3.4108	11.6338	2.0645	17.4295	0.8597	-0.1333
F10.7	2.2039	4.8570	1.4413	13.0032	0.9402	-0.0139
Mg II CWR	2.0706	4.2874	1.4044	12.8850	0.9475	-0.0379
Lyman-Alpha	2.2157	4.9094	1.4568	13.0893	0.9402	-0.0597
S10.7	2.064	4.2600	1.3516	12.2320	0.9489	-0.0135
Solar S10.7	2.1577	4.6557	1.4274	12.9051	0.9419	-0.0538
Corrected F10.7	2.5432	6.4679	1.6436	14.8091	0.9106	-0.0704
P10.7	2.1587	4.6598	1.4198	12.8312	0.9420	***0.0092***
E10.7	2.3204	5.3841	1.5038	13.7618	0.9334	-0.1104
FISM2 EUV	***1.9539***	***3.8177***	***1.3120***	***11.9038***	***0.9537***	-0.0269

Table 1. Error evaluation of the solar flux proxies for 2000 - 2019 at 45°E, 0°N. The error value corresponding to the best performing proxy in each column is in bold and italic. For all metrics besides the mean of the difference between data and model, the model which uses FISM2 EUV performs the best.

few days) were present in the original dataset. To account for these outlier cases, the model is built in two iterations. This involves constructing the model at each location twice in succession. After the first iteration, points satisfying the following criteria are removed from the set:

1. Data-model percentage difference exceeds 2 standard deviations.
2. Solar flux (using FISM2 EUV) and relevant delays remain below 6.5 mW/m^2
3. Geomagnetic index (Ap_3) and relevant delays remain below 80.

4 Investigation of Solar Flux Proxies

A significant task of the current study is to determine the most suitable solar flux proxy out of those described in section 2.3 to use as input to the model. The data themselves show noticeable differences, as displayed in Figure 2. In particular, the relative strengths of solar cycles 23 and 24 vary largely depending on proxy. For $F_{10.7}$, $S_{10.7}$, $P_{10.7}$, FISM2 EUV, TIMED SEE EUV, Lyman-alpha, and the Mg II core-to-wing ratio, the peak of solar cycle 23 (occurring, according to monthly sunspot number, in November 2001) is slightly stronger than that of solar cycle 24 (April 2015). The best-performing models typically use these data as their solar flux parameters. In the corrected $F_{10.7}$, the two solar cycles show similar maximum activity. Finally, SOHO EUV, the raw $S_{10.7}$ index, and especially the $E_{10.7}$ index predict significantly higher activity during the peak of solar cycle 23. Only the TIMED SEE EUV data are not available for the entire 2000 to 2019 epoch, having begun operations in January 2002.

For each proxy, the same terms were included as parameters in the model: real-time, 24-hour delay, 192-hour (8 day) delay, 576-hour (24 day) delay, and 864-hour (36 day) delay terms. The real-time solar flux parameter included both linear and quadratic terms; the delay terms were only linear. The model was developed twice for each solar flux proxy: once from 2002-2019, once from 2000-2019. This was done in order to provide a meaningful comparison of the TIMED SEE EUV data to the other chosen solar flux indices. Several error metrics were used to evaluate the performance of these developed models, including the root mean squared error (RMSE), mean squared error (MSE),

	RMSE (TECu)	MSE ($TECu^2$)	MAE (TECu)	MAPE	Correlation Coefficient	Mean of Data-Model Difference (TECu)
TIMED EUV	1.7473	3.0532	1.2279	12.5472	0.9397	-0.0030
SOHO EUV	2.7853	7.7576	1.7292	16.4171	0.8602	-0.1153
F10.7	1.8460	3.4075	1.2683	12.8598	0.9411	0.0091
Mg II CWR	1.8402	3.3863	1.2592	12.7875	0.9422	-0.0673
Lyman-Alpha	1.9153	3.6684	1.2894	12.9100	0.9363	-0.074
S10.7	***1.7272***	***2.9831***	1.1884	12.0422	***0.9486***	-0.0242
Solar S10.7	1.8502	3.4232	1.2631	12.7769	0.9357	-0.0359
Corrected F10.7	1.9795	3.9183	1.3743	14.1752	0.9107	-0.0452
P10.7	1.8074	3.2667	1.2504	12.6814	0.9431	***-0.0016***
E10.7	1.9944	3.9775	1.3361	13.5732	0.9267	-0.0972
FISM2 EUV	1.7277	2.9848	***1.1717***	***11.8086***	0.9483	-0.0288

Table 2. Error evaluation of the solar flux proxies for 2002 - 2019 at 45°N, 0°E. The error value corresponding to the best performing proxy within each column is in bold and italic. For RMSE, MSE, and the correlation coefficient, the model which uses $S_{10.7}$ performs the best. For MAE and MAPE, FISM2 EUV produces the best-performing model. For the mean of the difference between data and model, the $P_{10.7}$ index produces the best-performing model.

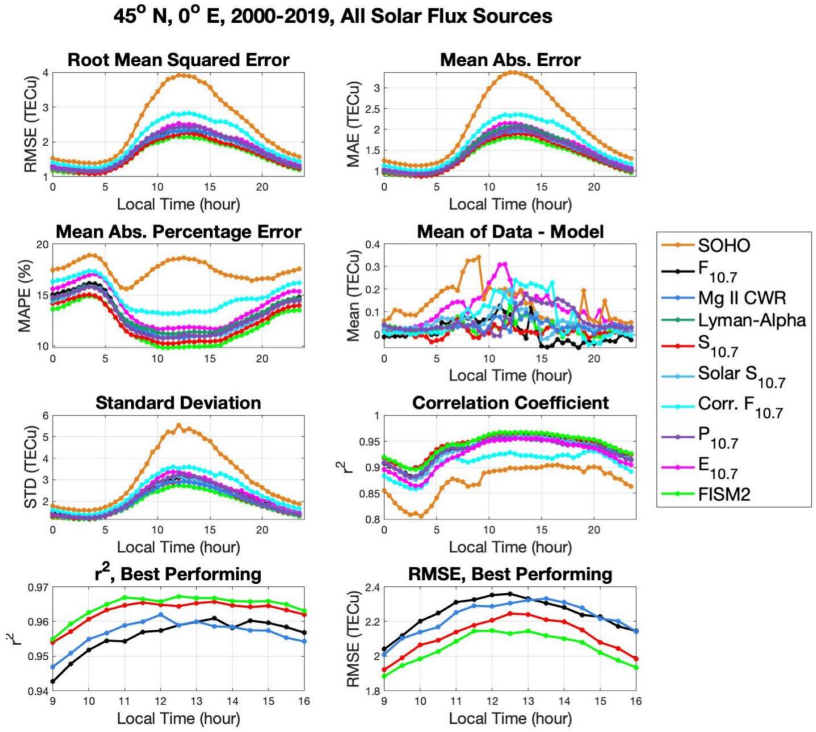

Figure 4. A comparison of the performance of solar flux proxies with a dependence on local time for 2000 - 2019.

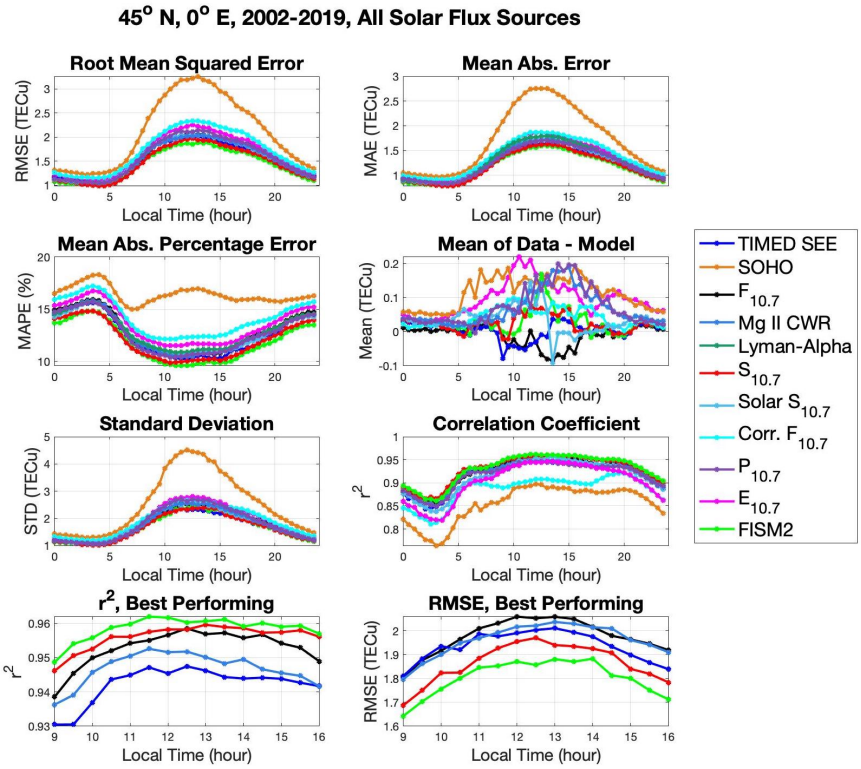

Figure 5. A comparison of the performance of solar flux proxies with a dependence on local time for 2002-2019.

mean absolute error (MAE), mean absolute percentage error (MAPE), correlation coefficient (r^2), and the mean of the data-model difference. The results of error analysis for 45^{o}N 0^{o}E are shown in Table 1 for the entirety of the TEC dataset (2000 - 2019) and in Table 2 for the years covered by the TIMED SEE EUV data (January 2002 - 2019). We note that the errors in 2002-2019 epoch are clearly lower than in 2000-2019. This is most likely related to higher solar activity in 2000-2001 and, consequently, higher absolute TEC values during those years. In addition, model errors are evaluated with a dependence on LT, as shown in Figure 4 for the 2000 - 2019 epoch and Figure 5 for the 2002 - 2019 epoch. Diurnal variation in the accuracy of the model is clearly evident for all solar flux proxies, with the largest absolute errors typically observed around 12 - 13 LT and smallest errors around 5 LT, reflecting maximum and minimum values of total electron content.

Clear differences are observed in the relative performance of each solar flux proxy. For the model which includes data from 2000 to 2019, the best-performing are the FISM2 EUV, the $S_{10.7}$ index, the solar $S_{10.7}$ index, and the Mg II core-to-wing ratio. As $F_{10.7}$ has been traditionally the most-used solar flux proxy, we include this proxy for comparison in lieu of solar $S_{10.7}$ in the bottom panels of Figure 4. $P_{10.7}$ is excluded from these panels, as well, on account of its modest performance in conjunction with the philosophical dilemma in its use described above. In comparing the model to the data on which it is built, the best-performing four proxies have root mean squared error below 2.2 TECu, mean squared error below 4.66 TECu, mean absolute error below 1.43 TECu, and cor-

relation coefficient above 0.94. These results are consistent with conclusions of Maruyama (2010), who investigated five types of solar flux proxies and concluded that the $S_{10.7}$ index outperforms $M_{10.7}$ and $F_{10.7}$ for TEC modeling over Japan. The Mg II core-to-wing ratio also performs better than $F_{10.7}$ in application to our ionospheric model. This also agrees with the claim made by Viereck et al. (2001) in their suggestion that the Mg II data is more suitable than $F_{10.7}$ as a proxy for the solar extreme ultraviolet flux, a suggestion made based on data from 1978 to 2000.

The model built with TIMED SEE EUV data performs well, though we will mostly consider only those proxies available for the longer time period (including all of years 2000 and 2001). The TIMED data do not outperform the other indices to an extent which warrants neglecting a large part of the maximum corresponding to solar cycle 23. Even for the 2002 - 2019 period covered by the TIMED SEE data, there are frequent data gaps listed by T. N. Woods (2005). Many of these are attributed to the TIMED SEE "Safe Mode." In terms of r^2, for daytime hours, TIMED SEE EUV rivals the SIP $E_{10.7}$. This is expected, as the two proxies represent roughly the same wavelength range and the removal of the time period not covered by TIMED SEE avoids the sharp peak in $E_{10.7}$ observed in Figure 2(j). SIP v2.38 was derived mostly with the correspondence of indices and proxies to the TIMED SEE v11 data. In terms of RMSE, for the 2002 - 2019 period, the TIMED SEE EUV performs better than all proxies except $S_{10.7}$ and FISM2 EUV. Regardless, FISM2 EUV outperforms TIMED SEE EUV and other proxies in terms of all error metrics and does not suffer from the data gaps shown by TIMED SEE EUV, making FISM2 EUV the most appropriate choice of solar flux proxy as input to the model.

As shown in Figure 4, the model built using SOHO SEM EUV is generally the worst-performing. This is evident across all error metrics used with the exception of the mean of the data-model difference. Although the reason for this is not clear, we note that the ratio between solar maxima 23 and 24 for SOHO SEM solar flux is higher than for other formulations of solar flux. In addition, the SOHO SEM flux during the solar minimum 2018-2019 is lower than during the solar minimum of 2008-2009 (see Figure 2). While we cannot completely rule out some uncorrected degradation of the SEM data during the last several years, comparison of SOHO SEM with SDO EVE measurements shows good agreement of observations at least until the end of 2013 (Wieman et al., 2014).

To indicate an overall relationship between TEC and different solar data, Figure 6 presents a relative deviation in the ratio TEC_{mod}/F_{sol} for four of the best-performing formulations of solar flux at 6 LT (top) and 15 LT (bottom). The relative deviation is determined as

$$\Delta\frac{TEC_{mod}}{F_{sol}} = \frac{\frac{TEC_{mod}}{F_{sol}} - (\frac{TEC_{mod}}{F_{sol}})_{mean}}{(\frac{TEC_{mod}}{F_{sol}})_{mean}} \tag{11}$$

where TEC_{mod} is the TEC value provided by the model and F_{sol} is the solar flux proxy used in that model. We note that the same behavior in relative deviation is seen in TEC observations, though it is more clear in the modeled TEC. For 6 LT, relative deviation is simple and shows a strong annual variation, with wintertime minimum and summertime maximum, and a weak solar activity dependency. For 15 LT, the relative deviation is more complex and is dominated by two main features: solar activity variation and seasonal variation. Positive values are seen for high solar activity levels and negative values for lower solar activity levels, probably reflecting the non-linear nature of TEC response to increases in solar flux. The seasonal response is more complex and shows a minimum in TEC_{mod}/F_{sol} in winter and two peaks during the equinoxes. This behavior reflects an annual variation in TEC with lower TEC in winter than in summer, and a semiannual variation in TEC which is partially related to semiannual variation in neutral composition and density. All four formulations of solar flux show these features, though dependence on solar activity level is strongest for the $MgII$ index and

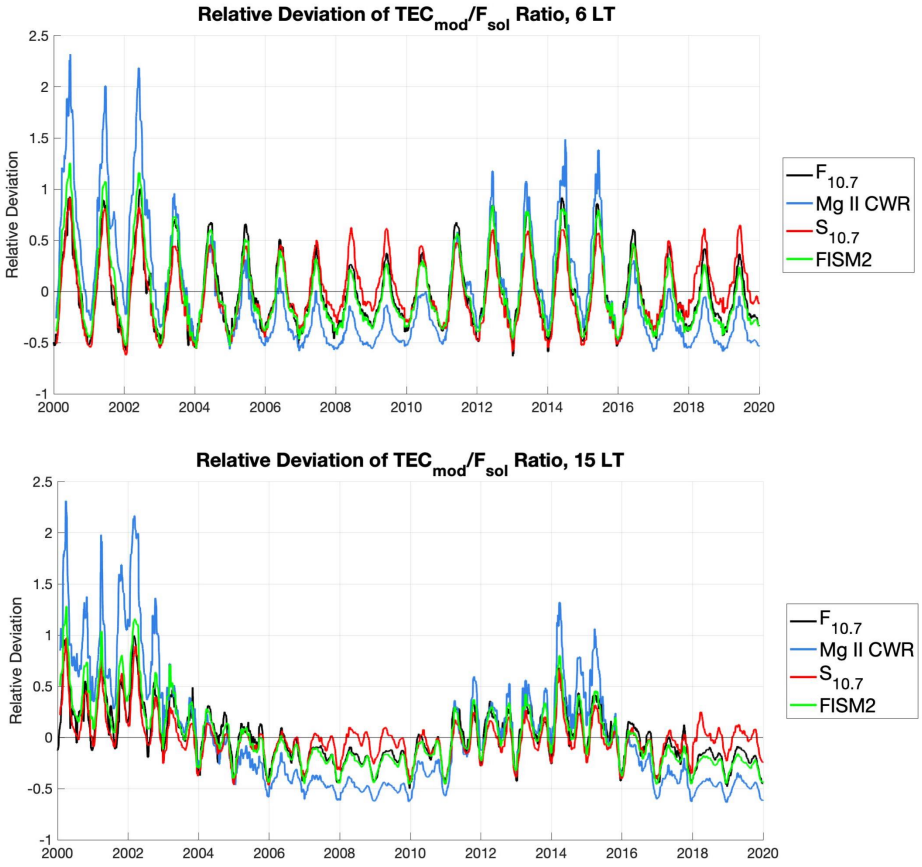

Figure 6. Relative deviation of TEC_{mod}/F_{sol} ratio for different solar flux proxies at 6 LT (top) and 15 LT (bottom).

weakest for the $S_{10.7}$ index. In developing the $S_{10.7}$ index, SET artificially removes about 30% of the energy at the top of the atmosphere during solar minimum by reducing the solar value of $S_{10.7}$ in order to correct for thermospheric cooling and to best match the orbital drag above 200 km for the NORAD catalog, where $S_{10.7}$ is primarily used in operations. Apparently, this adjustment affects the TEC values as well, as the $S_{10.7}$ index is found to perform very well for TEC modeling and only slightly worse than FISM2 EUV.

To summarize, our analysis of the several formulations of the model differing only in the solar flux proxy suggest that FISM2 EUV is statistically the best choice to use in the final formulation of the model. Models built with this proxy outperform those developed with datasets traditionally used to reflect solar activity, $F_{10.7}$ in particular. Not only does FISM2 EUV show that it is the most appropriate proxy to use through statistical analysis, but also according to physical application to the system being modeled. These data are developed to directly reflect the solar output between 0.05 to 105.05 nanometers. This includes the 26 to 34 nanometer range, the subset of the extreme ultraviolet range absorbed by atomic oxygen above 200 kilometers (W. K. Tobiska et al., 2008), [IS 14222] which corresponds mostly to the F-region ionosphere. From a physical point of view, it is reasonable that an index reflecting the solar irradiance in the bandwidth responsible for a large portion of ionization in the ionosphere (in addition to other wavelengths in the EUV range) should produce the best-performing model. $S_{10.7}$ reflects the 26 to 34 nanometer range, but does not cover other potentially relevant wavelengths in the EUV range. FISM2 EUV, therefore, is ultimately the dataset used to characterize solar flux in the final formulation of the model. For historical purposes and for comparison with other models, we also retained the version of the model using $F_{10.7}$, as $F_{10.7}$ proxy has been traditionally used for thermospheric and ionospheric modeling.

5 Evaluation of Model Performance

5.1 Performance Metrics

It was concluded in Section 4 that the model with FISM2 EUV as a solar flux index performs better than with other solar flux surrogates. In this section we examine in more detail performance of the model with the FISM2 EUV data. A variety of metrics are used to examine different features in the models' performance, with several of them already presented in Figures 4 and 5. The top panel of figure 7 shows a scatter plot of the observed and modeled TEC for all conditions, together with a linear fit and several performance metrics. The RMSE of the model is 1.9539 TECu. We note that this is lower than RMSE = 2.5-3.0 TECu obtained by Feng et al. (2019) at mid-latitudes, even though Feng et al. (2019) used highly smoothed IGS TEC maps with inherently lower variability in TEC data. In a study which is closer to our effort, when the empirical TEC model was constructed based on high-resolution observations over middle latitudes in Japan, the RMSE is equal to 3.3-3.4 TECu (Maruyama, 2010). The higher accuracy of our model is thought to result from a more detailed description of solar flux, seasonal and local time behavior, and inclusion of geomagnetic activity effects.

The bottom panel of Figure 7 shows a scatter plot of the observed and modeled TEC for all conditions for the model developed using $S_{10.7}$ as the solar flux input parameters. This is the second-best-performing model of those developed using the formulation for model construction defined here. The error metrics corresponding to this model are less favorable than those for the model developed using FISM2 EUV, though both models perform better than previous models referenced above which provide error metrics for this latitude (Feng et al., 2019; Maruyama, 2010).

Figure 8 illustrates the performance of the TEC model with season and local time using common error metrics such as mean absolute percentage error (MAPE, top), root mean square error (RMSE, middle), and root mean square percentage error (RMSPE,

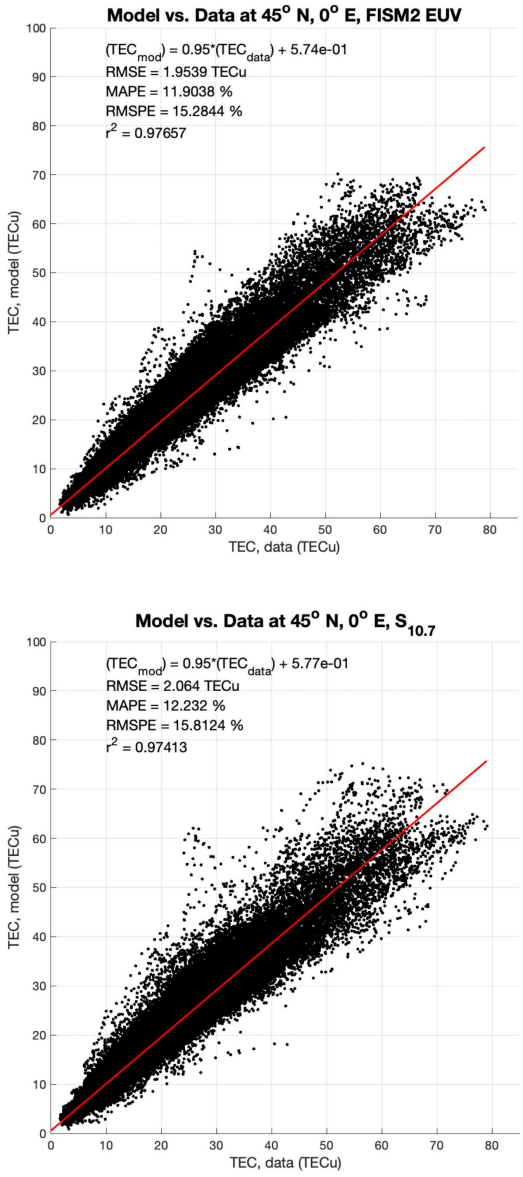

Figure 7. Scatter plot showing the relationship between observed and modeled TEC for the model built with FISM2 EUV as the solar flux proxy (top). Scatter plot showing the relationship between observed and modeled TEC for the model built with $S_{10.7}$ as the solar flux proxy (bottom).

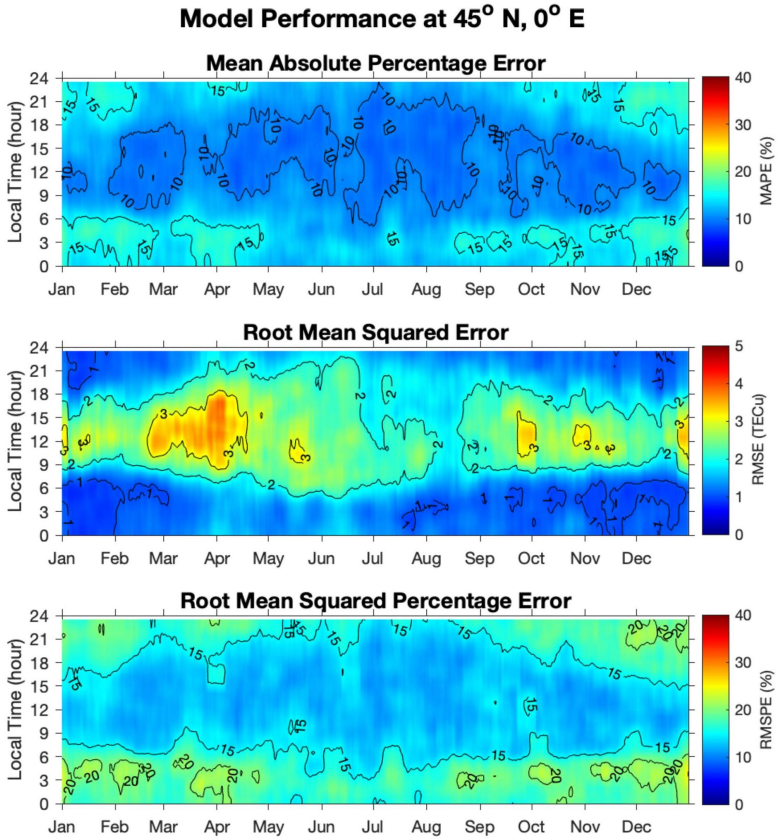

Figure 8. Performance of the TEC model in terms of mean average percentage error (MAPE, top), root mean square error (RMSE, middle) and root mean square percentage error (RMSPE, bottom) as a function of season and local time.

bottom). In figure 8, all metrics are calculated independently for each 30-min local time bin with a sliding 10-day window. The daytime MAPE is mostly within 8-13% for all seasons, indicating that the model does not have seasonal biases and properly reflects seasonal variation in TEC. The nighttime MAPE increases to 15-17% due to the decrease in TEC at night, but does not reach 20%. The RMSE variation (middle panel) shows the opposite local time behavior, again following diurnal variation in TEC, and varies mostly within 2-3 TECu for daytime and 0.5-1.5 TECu at night. The increase in RMSE in March-April and September- October is related to a combination of the semi-annual variation in TEC, i.e. equinoctial enhancement, and elevated levels of geomagnetic activity. The RMSPE closely follows the variation in MAPE and varies within 12-15% during daytime and 15-20% at night. Overall, the model does not show seasonal or local time biases, and seasonal or local time variations in considered metrics are consistent with such variations in TEC.

Figure 9 presents more details on fitting coefficients (left panels) and P values (right panels) for several terms reflecting geomagnetic activity (top) and solar flux (bottom). For geomagnetic activity, the largest coefficients are real-time Ap_3 and Ap_3 with a 3-hour delay; they reach maximum values during daytime hours (9-18 LT). Note that the coefficient for real-time quadratic Ap_3 is negative, thus decreasing the influence of real-time Ap_3. Overall, the combination of terms indicates positive coefficients for real-time Ap_3

and Ap_3 with 3-hour delay for daytime hours and mixed or negative results around dawn (3-7 LT), with a non-linear impact of Ap3 variations on TEC. This dependency corresponds to a positive storm effect (increase in electron density and, subsequently, in TEC) occurring at mid-latitude locations during daytime shortly after an increase in geomagnetic activity, and mixed or negative storm effect (decrease in TEC) after an increase in geomagnetic activity occurring at dawn. The positive ionospheric storms at middle latitudes are typically observed in the initial phase of the storm and are most likely to occur at longitudes that are in the ionization production dominated morning-noon local time sectors during the onset of geomagnetic storm (Prölss, 1995; Lu et al., 2008; Balan et al., 2010). Positive storm effects are driven by combined effects of equatorward wind and prompt penetration electric fields that lift the ionospheric plasma to higher altitudes with lower recombination rates. Our results are fully consistent with earlier studies of positive storm effects. Study of storm effects by Thomas et al. (2016) noted first emergence of weak negative storm effects 3-6 hours after the storm onset in the dusk and dawn regions. Our results of weak negative Ap_3 coefficients around dawn are also consistent with Thomas et al. (2016) study. We also note a pronounced 3-hr variation in coefficients for Ap_3 and Ap_3 with 3-hr delay; this variation has the opposite behavior (increase in the Ap_3 coefficient at a time of decrease of the coefficient for Ap_3 with 3-hour delay). This most likely reflects the competing nature of temporal delays in TEC to a geomagnetic storm and points to the shortcomings of the Ap_3 index; an index with higher temporal resolution than the 3-hr resolution of Ap_3 is required to better resolve TEC changes due to geomagnetic activity, as in the example of using Dst for 1-hour time resolution in the JB2008 model during storm periods. The coefficient for Ap_3 with 24-hour delay (black line in top left panel of Figure 9) is negative and highly significant (P values well below 0.05) for all local times. This corresponds to a well-known negative storm effect in the mid-latitude ionosphere occurring the day after a geomagnetic storm (Mendillo, 2006; Wood et al., 2016). The coefficient for Ap_3 with 48-hour delay is also negative and statistically significant for all local times. Moreover, we found that the coefficient for Ap_3 with 72-hour delay is statistically significant, especially for nighttime hours, although lower than the coefficient for Ap_3 with 24-hour delay. Physically, this corresponds to long-lasting negative storm effects that are weaker but still can be identified 48 hours and even 72 hours after the storm. Our empirical model is expected to capture these negative storm effects.

The dependence of TEC on solar flux (lower panels of Figure 9) is more straightforward. Coefficients and P values for FISM2 EUV and $S_{10.7}$, the solar flux indices which produce the best-performing models, are shown. Coefficients for real-time solar flux and all delays are positive for most local times, but largest for daytime hours, indicating an obvious connection: the increase in TEC in response to increase in solar radiation. For FISM2 EUV, a larger response is observed during daytime in the 24-hour delay term than in the real-time solar flux term. The opposite effect is observed for the $S_{10.7}$ coefficients. The combined effects of contributions from both linear and quadratic terms for real-time solar flux are lower during daytime than for FISM2 EUV with a 24-hour delay, and the two are comparable for nighttime from 0-6 LT. From 18-24 LT, the real-time linear and quadratic coefficients combined are larger than the 24-hour delay coefficients, the latter of which are negative from 21-24 LT. The real-time $S_{10.7}$ coefficients are lower than the 24-hour delay from 0-5 LT and higher from 18-24 LT; from 20-24 LT, the 24-hour delay term is negative as it was in the case of the FISM2 EUV.

Studies of the thermospheric response to the $S_{10.7}$ index found that thermospheric density correlates best with $S_{10.7}$ with a 24-hour delay (B. R. Bowman et al., 2008b), which is consistent with the atomic oxygen thermal conduction timescale in the thermosphere. Higher coefficients for the real-time $S_{10.7}$ index in our model for TEC represent the prevalence of a rapid response of ionospheric electron density to ionizing radiation. Longer time scales - in particular, solar flux with 24-hour delay and 192-hour, 576-hour, and 864-hour delays - represent the temporal scales of thermospheric response to ion-

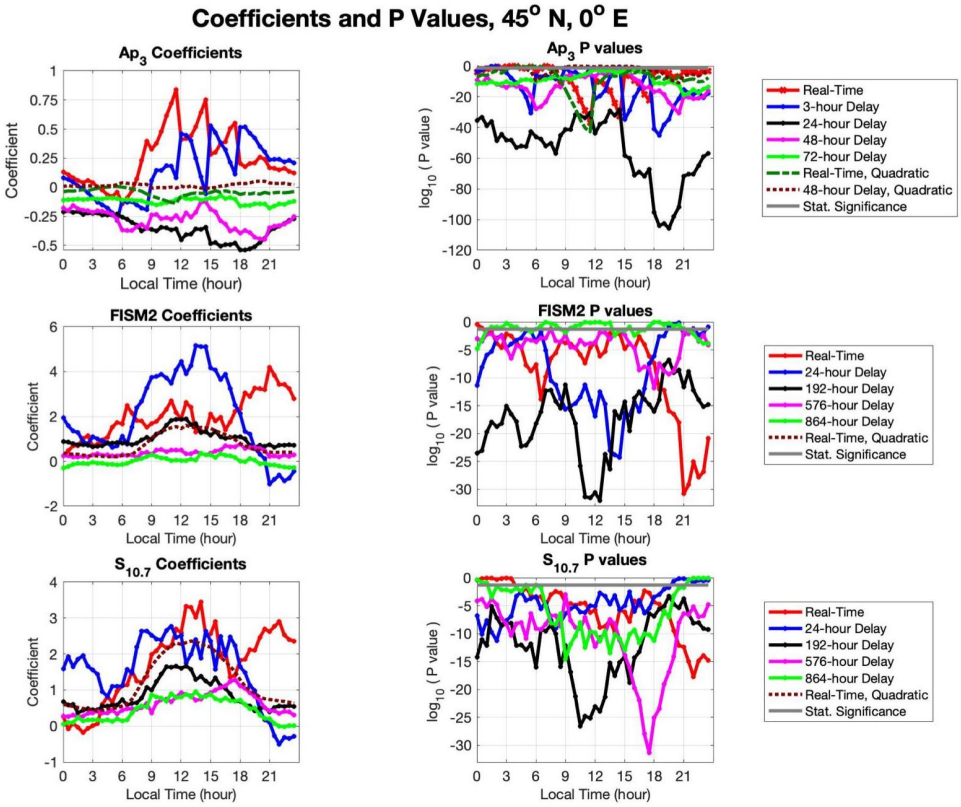

Figure 9. Modeling coefficients (left) and P values (right) for terms describing dependency on geomagnetic activity (top panels), FISM2 EUV (center panels), and $S_{10.7}$ (bottom panels). The two solar flux datasets are used to develop independent models and inserted here for comparison; the coefficients and P values corresponding to Ap_3 are mostly independent of the solar flux parameter used.

izing radiation. However, in the model with FISM2 EUV as the solar flux index, the 24-hour delay term has larger coefficients during daytime than real-time solar flux. This suggests a higher contribution from the delayed thermospheric response to ionizing radiation in this model. Maruyama (2010) has demonstrated that the delayed response of TEC to solar irradiance is different for different solar proxies; in their study, SSN and the $F_{10.7}$ proxy perform better with a 2-day delay, while the $S_{10.7}$ and Mg II indices performed better with a 1-day delay. Our study suggests that not only is the 1-day delay term significant for FISM2 EUV, but it is more so than for the real-time term. Our test also indicates that a temporal delay of 144 hours has some statistical significance for certain local times. However, this term does not lead to a marked increase in the performance of the model, and therefore was not included in the current version of the model. Delay terms of 48, 72, and 96 hours do not show statistical significance. Similar to Lean et al. (2016), we found that inclusion of solar flux terms with several delays decreases the need for 81-day smoothed values, as inclusion of an 81-day smoothed solar flux term does not improve the model. Several studies have indicated that the combined use of several proxies of solar activity improved the empirical model in comparison with a single proxy (Maruyama, 2010, 2011; Lean et al., 2016). We have not explored the use of the combined proxies in this study.

We also validate our model through comparison with TEC observations in the year 2020. As our model was developed using data collected in 2000-2019, observations in the year 2020 represent an independent dataset that was not used for model development. Figure 10 presents TEC observations (top panel), predictions from our model (middle panel), and data-model differences in TECu (bottom panel) for January - March 2020. Blue lines indicate variations in the FISM2 EUV index, while black lines indicate variations in Ap_3 index. We note that the Jan-Mar 2020 conditions represent very low solar activity and serve as an extreme case for comparison. Figure 10 shows that our model accurately captures diurnal variation in TEC, with peak TEC predicted for 12-15 LT, in agreement with observations. The model also properly describes seasonal variation, a gradual increase from low winter-time TEC to the equinoctial peak in late March. This time period also has several minor increases in geomagnetic activity, which nevertheless can produce significant ionospheric variations during low solar activity conditions. Our model properly captures the increase in daytime TEC observed on Feb 6-7 in response to a prolonged increase in geomagnetic activity (Ap_3 = 15-27, Kp = 3.0–4.0), and on Feb 18, 19, and 21 (Ap_3 = 18-27). It also describes reasonably well the ionospheric response to a short-lived increase in Ap_3 that was observed only at one Ap_3 value (Mar 19, Ap_3 = 32 at 1.5UT and Ap_3 = 9 at 4.5 UT). The largest data-model differences are observed in March and could be related to unresolved variations due to an increase in geomagnetic activity and/or due to ionospheric oscillations with multi-day periods. For example, upward propagating planetary waves with 5-6 day periods have maximum amplitudes during the equinox and could potentially affect electron density, especially for solar minimum conditions (Gu et al., 2018; Yamazaki et al., 2018; Qin et al., 2019). Our model is not expected to capture this type of influence on TEC. The RMSE for the entire 3-month period is 1.0022 TECu, in line with what would be expected for low solar activity. Overall, the model performs very well for these extreme solar minimum conditions and is expected to perform even better for more typical conditions.

Figure 11 presents a prediction of TEC variation with season and local time for different levels of solar activity and different formulations of the model, with the FISM2 EUV index (left panels) and $F_{10.7}$ proxy (right panels). The strongest feature in seasonal dependence is semiannual variation, with TEC peaks occurring in late March and mid-October for moderate and high levels of solar flux (bottom four panels). This semiannual variation in TEC is closely related to semiannual variation in thermospheric composition and density (Fuller-Rowell, 1998; Rishbeth et al., 2000; B. R. Bowman et al., 2008b; Jones et al., 2018) and has been historically reported in ionospheric data (Richards (2001) and references therein). For moderate to high levels of solar flux, TEC is higher

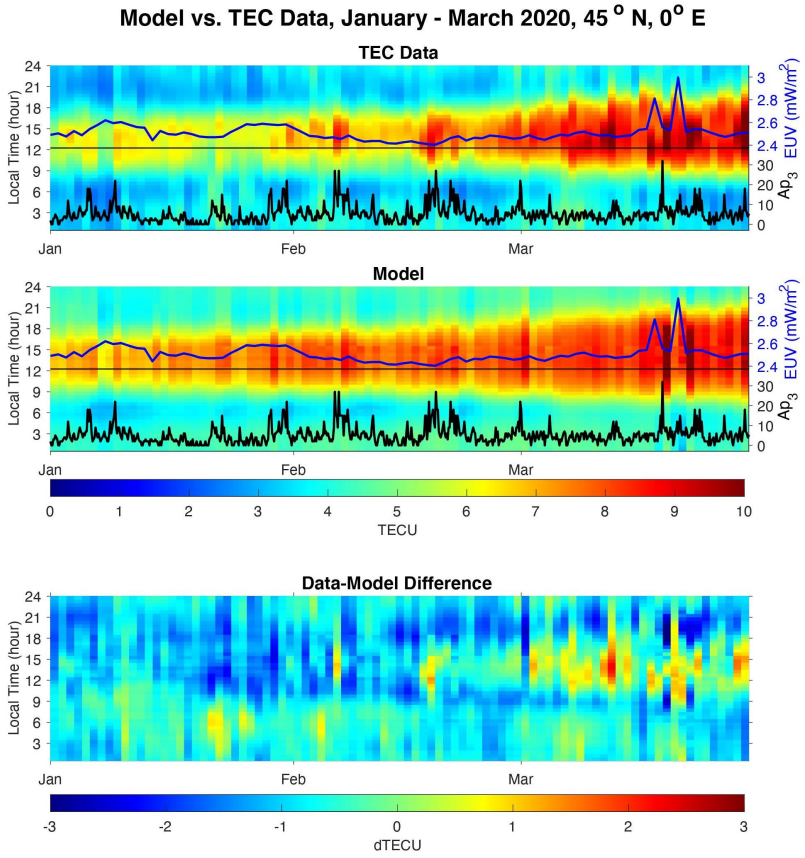

Figure 10. TEC observations (top), model predictions (middle) and data-model difference (bottom) for January-March 2020. Variations in FISM2 EUV (blue line) and Ap_3 index (black line) show that this period had extremely low solar activity with several minor geomagnetic disturbances.

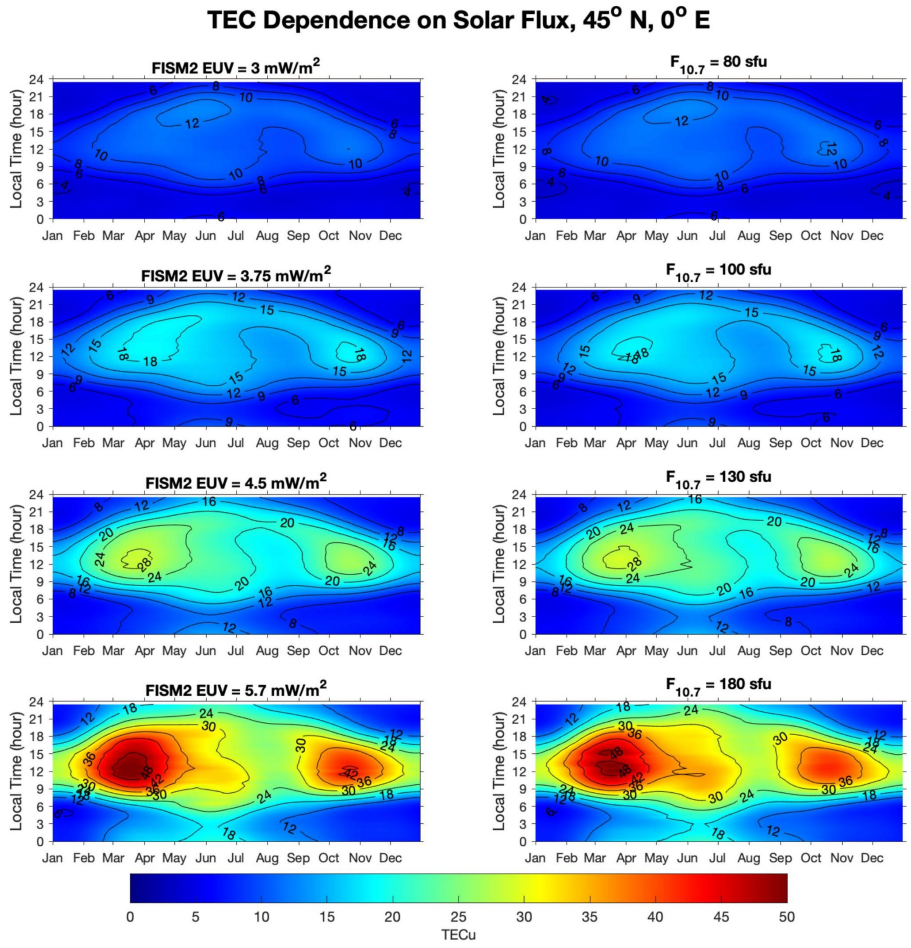

Figure 11. Model predictions of TEC variations with season and local time for different levels of solar activity. Left panels show the output for a model using FISM2 EUV, right panels show a model using $F_{10.7}$ index

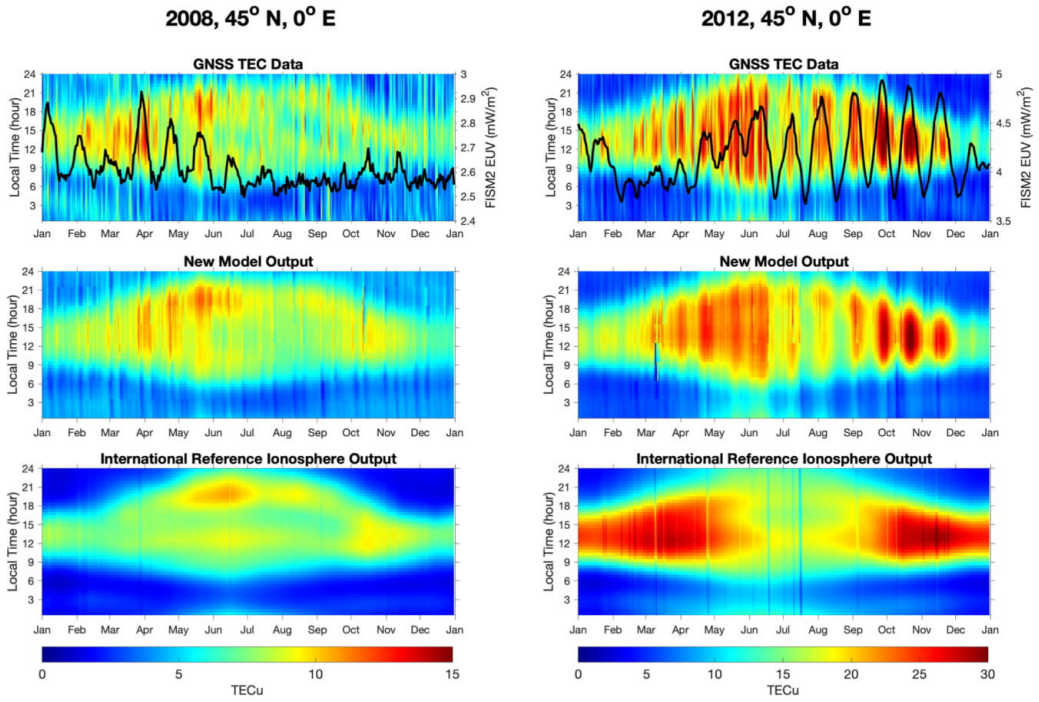

Figure 12. A comparison of GNSS TEC data (top panels), new model output (middle panels), and IRI-2016 output (bottom panels) for 2008 (left column) and 2012 (right column) at 45°N, 0°E. The FISM2 EUV for 2008 and 2012 is included for comparison to periodic fluctuations in TEC output.

during the spring equinox than during the fall equinox; this feature has been observed in, for example, COSMIC data (Burns et al., 2012). For moderate to high solar flux, peak values of TEC are predicted around local noon for winter and equinox conditions. However, for summer conditions, morning (8-11 LT) and evening (17-19 LT) peaks are predicted starting in May and June, shifting to a well pronounced evening peak in July through September. This local time behavior is particularly well pronounced for low solar flux conditions (top panels), when it dominates seasonal variation to the point where March peak in TEC does not develop. Overall, the new TEC model properly predicts numerous ionospheric features that are consistent with previous observations of ionospheric variations with solar flux, season, and local time. This demonstrates the utility of the model for in-detail studies of such features.

5.2 Comparison with International Reference Ionosphere

The International Reference Ionosphere (IRI, available at `irimodel.org`) provides an empirical model of the ionosphere with outputs of monthly averages of the electron density, electron temperature, ion temperature, ion composition, and other parameters between 50 and 2000 kilometers altitude (Bilitza, 2004; Bilitza et al., 2014, 2017). The model is a result of the long-term effort by international research community and collaboration between the Committee on space Research (COSPAR) and the International Union of Radio Science (URSI).

For comparison to our model, we use the most recent version, IRI-2016. The 2012 update to the IRI model had previously provided improvements in the representations of electron density, electron temperature, and ion composition according to Bilitza et al. (2014). These improvements are attributed to updates in ionosonde design and data analysis techniques, including, notably, the representation of seasonal and solar flux variability response. The IRI-2016 model also uses $F_{10.7}$, the sunspot number (R), and the ionosonde-based ionospheric global index (IG) as solar flux and ionospheric indices (Bilitza et al., 2017). Major improvements of IRI-2016 over IRI-2012 are described by Bilitza et al. (2017) and include new model options for $h_m F_2$ and an improvement of the representation of topside ion densities at the extremes of solar activity. In addition, this update includes progress in developing the IRI Real-Time model. Few differences are observed between IRI-2012 and IRI-2016 in terms of the structure of TEC output.

The IRI-2016 model includes $F_{10.7}$ and F_{81} (the 81-day averaged $F_{10.7}$ using 40 days prior to and following the date in question) as an optional input. Varying these parameters does not change the output of the model significantly, however, as IRI uses the 12-month running means of an ionosphere-effective solar index (IG12), sunspot number (Rz12), and other solar flux proxies as the default values to capture variations in solar flux (Gulyaeva et al., 2018).

Figure 12 shows the comparison between the GNSS TEC data, our model output, and the IRI-2016 output for a year of low solar flux (2008, left panel) and high solar flux (2012, right panel). FISM2 EUV data, used as the solar flux input to our model, is plotted in the top panels as a black line. Several notable differences are present.

The most significant difference observed is the presence of short-term fluctuations in TEC in our model and the raw data, particularly during a high solar flux year such as shown in the right panel of Figure 12. This periodicity in TEC shown in the data and our model appears to match the solar rotation period of 27 days. The IRI model does not show this periodicity, presumably because of a lower direct dependence on solar flux. The difference is less present in a low solar flux year, as represented in the left panel of Figure 12.

We compare the local time dependence of TEC in the data, new model, and IRI-2016. The right panel of Figure 12 shows that, during a year of high solar flux (2012), the spring and autumn peaks in TEC occur around 12 LT for the data and both models. During a low solar flux year (2008), an early-April peak in TEC occurs in the data and new model around 12 - 14 LT (Figure 12, left panel). IRI-2016 does not predict this peak, and in fact shows little LT variation in TEC at this point in the year, possibly because it does not capture the ionospheric response to a short-term increase in solar flux as shown in the left panel of Figure 12. Both IRI-2016 and our model correctly predict a second peak in TEC that occurs around 18 - 22 LT in May through September. Another local time peak in the late spring and summer, observed at 9 - 10 LT, is well predicted by our model. However, IRI expects it to occur later, around 12 LT. The autumn peak for the data and both models is relatively consistent in LT, occurring around 12 - 14 LT. Under low solar flux conditions, the IRI model generally underestimates nighttime TEC values, while our model represents them well. During the spring of a high-solar flux year, the IRI model overestimates daytime TEC, while underestimating daytime TEC from June to August. Our model shows a significant improvement in prediction of TEC during these times.

Differences in seasonal variation are also present. For a year of low solar flux (2008), IRI predicts twice-daily enhancement in TEC in June, and a fall equinox peak in mid-October around 12 - 14 LT. Our model reflects similar seasonal peaks but captures another period of elevated TEC in April which corresponds to an increase in solar flux. For a year of high solar flux, as shown in the right panel of Figure 12, the spring peak in IRI is both earlier and more substantial than in either our model or the TEC data. IRI shows

a higher peak in TEC centered around mid-March, whereas the most elevated TEC in the new model and data occurs later, in late May and early June. The autumn peak in TEC as predicted by IRI is slightly later in the year, in early to mid November, whereas the data and model show an autumn peak in mid-October. Perhaps most notably, IRI overestimates daytime TEC during the winter months (December, January, and February in particular) during the year of high solar flux. Our model describes TEC levels during these months well.

Similar limitations in the predictions made by the IRI model are described in other studies. Li et al. (2016) make a comparison similar to ours above, but for the years 2009 and 2013, using IRI-2012 to TEC-GIM maps at the mid-latitude Beijing Fangshan station (BJFS) in China (39.6^o N). They note that the periodicity of TEC-IRI more closely resembles TEC-GIM during the low solar flux year, while during a high solar flux year, main differences between GIM and IRI-2012 may be largely attributed to periodic (annual, semiannual, three-monthly, and four-monthly) components and the solar activity component. Nighttime underestimation and daytime overestimation of TEC by IRI-2012 during a high solar flux year are also noted. In this study, the IRI-2012 solar activity component shows very little variation over the course of the year, and the IRI-2012 dependence on periodic components is strongly muted when compared to GIM-TEC. Large differences are observed, in particular, between the TEC-GIM and TEC-IRI annual and three-monthly components during 2013. This suggests that the inclusion of a major dependence on both periodic and solar activity components may yield better agreement with the data, particularly during years of relatively high solar flux. Similar patterns are observed in comparison of IRI-2016 to our model and the GNSS TEC data, as described above.

As described by Tariku (2016), who studies IRI-2012, this version tends to underestimate TEC at mid-latitudes during years of low solar flux, and often overestimates the data during years of higher solar flux. In a comparison of IRI-2016 and IRI-2012 to TEC data over mid-latitude locations in the continental United States, Tariku (2019) notes that IRI-2016 is better able to estimate TEC during evening hours than IRI-2007 and IRI-2012, but largely overestimates TEC when solar flux increases during the day. This is particularly clear during periods of low solar flux, including the December solstice. Differences between IRI-2012 and IRI-2016 are attributed to IRI-2012's omission and IRI-2016's subsequent addition of the plasmaspheric TEC, which contributes to overall TEC more significantly during nighttime (Kumar, 2016). Zakharenkova et al. (2015) similarly shows that the IRI-Plas model, an extension of IRI accounting for plasmaspheric contributions prior to the development of IRI-2016, overestimates TEC at middle latitude even during periods of low to moderate solar flux. The limitations of IRI-2016 are attributed to the new model options in estimating h_mf_2 directly as well as the improved representation of topside ion densities at extremes of solar activity, as discussed in (Bilitza et al., 2017; Tariku, 2019). Of particular concern to Kumar (2016) is the difference between EUV (particularly 26 - 34 nm) and the solar flux parameters used in the IRI model; in IRI-2012, the TEC output depends on N_mf_2 and h_mf_2, which depend on IG12 and Rz12 respectively. Many sources cite that differences between IRI-TEC and TEC data tend to be less significant at mid-latitudes than low and high latitudes (Kumar, 2016; Kumar et al., 2015; Alcay et al., 2017).

Our model addresses several of the limitations of IRI addressed by these studies and our discussion above. Most notably, the 27-day periodic variations in TEC during years of high solar flux are well captured by our model, while both IRI-2012 (Li et al., 2016) and IRI-2016 fail to describe it. Our model captures the daytime and nighttime amplitude as well as the seasonal and local time position of the TEC peak, a notable improvement over the nighttime underestimation, daytime overestimation, and seasonal and local time limitations of IRI.

6 Summary

Development of forecasting capabilities of the near-Earth space environment remains one of the important topics in space weather research. As the accuracy of existing empirical models falls short of what is required to meet the needs of space weather services and the needs of academic research community, development of new empirical models with increased accuracy and spatio-temporal resolution is required.

This work presents the first stage in the development of a new empirical TEC model that aims to provide high temporal and spatial resolution. The model is formulated at a single location, 45^oN and 0^oE, and aims to accurately describe variations in TEC with solar cycle, season, LT, and geomagnetic activity with 30-min resolution. The model is constructed using 20 years of high-resolution TEC observations from the CEDAR madrigal database (2000-2019) and uses multiple temporal delays (ranging from 24 hrs to 36 days for solar flux and from 3 hrs to 72 hrs for geomagnetic activity) to describe TEC dependence on solar EUV and geomagnetic activity.

The central focus of the current work is investigation of different descriptions of solar flux proxies with the goal to select the most appropriate proxy to describe TEC variations. This study examined 11 descriptions of solar flux surrogates and measurements (TIMED SEE EUV, SOHO EUV, $F_{10.7}$, the Mg II core-to-wing ratio, the Lyman-alpha composite, $S_{10.7}$, raw $S_{10.7}$, corrected $F_{10.7}$, $P_{10.7}$, $E_{10.7}$, and FISM2 EUV) for two time periods, 2000-2019 and 2002-2019, using the same formulation of the empirical model. Our results indicate that the FISM2 EUV index performs the best, closely followed by the $S_{10.7}$ index, the $F_{10.7}$ proxy, and the Mg II index. As inclusion of the years 2000 to 2001 is important for proper description of TEC variations during high solar activity, the absence of TIMED EUV data prior to 2002 limits its applicability.

The overall RMSE of the model is 1.9539 TECu, lower than that of comparable empirical models. The RMSE of the new empirical model varies within 0.5-1.5 TECu at night and 2-3 TECu during the daytime. MAPE (Mean Absolute Percentage Error) varies within 8-13% during daytime and within 15-17% at night, without seasonal biases. Higher accuracy is attributed to the combined influences of more accurate descriptions of TEC dependency on solar flux, season, local time, and geomagnetic activity.

The model represents well features such as changes in TEC with solar activity, season, and LT, semiannual variation in TEC, and stronger enhancement in TEC in March as compared to October.

The new empirical model properly captures several features that are not well represented by IRI-2016, in particular wintertime TEC for moderate to high solar flux, and LT variations of TEC for low solar flux conditions. However, the largest strength of our model in comparison with IRI-2016 is an accurate description of TEC variation in response to short-term changes in solar flux.

Future efforts envision extension of the modeling approach to other longitudes and latitudes, as well as inspection and introduction of additional space weather and meteorological drivers.

7 Acknowledgements

L.P.G. and C. T. acknowledge support of this study from NASA grant 80NSSC19K0262. L. P. G., A. J. C., S. R. Z. and C. T. also acknowledge funding from the ONR Grant N00014-17-1-2186. C.T. gratefully acknowledges support from the US National Science Foundation (NSF) REU (Research Experience for Undergraduates) program grant AST-1659420 to the Massachusetts Institute of Technology (MIT) Haystack Observatory that funded his effort in summer 2019. TEC data processing and research activities at MIT Haystack

Observatory are supported by US NSF grant AGS-1952737. W. K. T. acknowledges support from SPAWAR contract N6600120P6336 for the production of the S10, M10, and Y10 indices.

All of the data used in this paper are publicly available. GPS TEC data products and access through the CEDAR Madrigal distributed data system (`http://cedar.openmadrigal.org/`) are provided to the community by the MIT Haystack Observatory. The $F_{10.7}$ proxy and Ap_3 index are also available from (`http://cedar.openmadrigal.org/`). The Mg II core-to-wing ratio is available at (`http://www.iup.uni-bremen.de/UVSAT/Datasets/mgii`). $S_{10.7}$ index data is provided by (`https://sol.spacenvironment.net/JB2008/`). $E_{10.7}$ index is provided by Space Environment Technologies (SET) (`http://www.spacewx.com/solar2000.html`. The SOHO SEM EUV data are made available by USC Dornsife (`https://dornsifecms.usc.edu/space-sciences-center/download-sem-data/`). The FISM2 EUV and Composite Lyman-alpha data are available from the LASP Interactive Solar Irradiance Data Center (`http://lasp.colorado.edu/lisird/`). The TIMED SEE data are available from the University of Colorado at Boulder Laboratory for Atmospheric and Space Physics (LASP) website (`http://lasp.colorado.edu/home/see/data/`).

Data for TEC processing is provided from the following organizations: UNAVCO, Scripps Orbit and Permanent Array Center, Institut Geographique National, France, International GNSS Service, The Crustal Dynamics Data Information System (CDDIS), National Geodetic Survey, Instituto Brasileiro de Geografia e Estatística, RAMSAC CORS of Instituto Geográfico Nacional de la República Argentina, Arecibo Observatory, Low-Latitude Ionospheric Sensor Network (LISN), Topcon Positioning Systems, Inc., Canadian High Arctic Ionospheric Network, Centro di Ricerche Sismologiche, Système d'Observation du Niveau des Eaux Littorales (SONEL), RENAG : REseau NAtional GPS permanent, GeoNet - the official source of geological hazard information for New Zealand, GNSS Reference Networks, Finnish Meteorological Institute, and SWEPOS - Sweden.

The authors acknowledge the MATLAB interface to IRI-2016 that was used in this study and available at `https://github.com/space-physics/IRI2016`.

References

Aa, E., Zhang, D., Ridley, A. J., Xiao, Z., & Hao, Y. (2012). A global model: Empirical orthogonal function analysis of total electron content 1999-2009 data. *Journal of Geophysical Research: Space Physics*, *117*(A3). doi: 10.1029/2011ja017238

Alcay, S., Oztan, G., & Selvi, H. (2017). Comparison of IRI_PLAS and IRI_2012 model predictions with GPS-TEC measurements in different latitude regions. *Annals of Geophysics*, *60*(5). doi: 10.4401/ag-7311

Balan, N., Shiokawa, K., Otsuka, Y., Kikuchi, T., Vijaya Lekshmi, D., Kawamura, S., ... Bailey, G. (2010). A physical mechanism of positive ionospheric storms at low latitudes and midlatitudes. *Journal of Geophysical Research: Space Physics*, *115*(A2).

Banks, P., & Kockarts, G. (1973). Aeronomy - part a. *Academic Press, New York and London*.

Bilitza, D. (2004). A correction for the IRI topside electron density model based on Alouette/ISIS topside sounder data. *Advances in Space Research*, *33*(6), 838–843. doi: 10.1016/j.asr.2003.07.009

Bilitza, D., Altadill, D., Truhlik, V., Shubin, V., Galkin, I., Reinisch, B., & Huang, X. (2017). International Reference Ionosphere 2016: From ionospheric climate to real-time weather predictions. *Space Weather*, *15*(2), 418–429. doi: 10.1002/2016sw001593

Bilitza, D., Altadill, D., Zhang, Y., Mertens, C., Truhlik, V., Richards, P., ...

Reinisch, B. (2014). The International Reference Ionosphere 2012 – a model of international collaboration. *Journal of Space Weather and Space Climate*, *4*. doi: 10.1051/swsc/2014004

Bouya, Z., Terkildsen, M., & Neudegg, D. (2010). Regional GPS-based ionospheric TEC model over Australia using Spherical Cap Harmonic Analysis. In *COSPAR Scientific Assembly 2010: 38th COSPAR Scientific Assembly, Bremen, Germany, 18-25 July 2010: Abstracts* (p. 4). COSPAR.

Bowman, B., Tobiska, W. K., Marcos, F., Huang, C., Lin, C., & Burke, W. (2008a). A new empirical thermospheric density model JB2008 using new solar and geomagnetic indices. *AIAA/AAS Astrodynamics Specialist Conference and Exhibit*. doi: 10.2514/6.2008-6438

Bowman, B. R., Tobiska, W. K., & Kendra, M. J. (2008b). The thermospheric semiannual density response to solar EUV heating. *Journal of Atmospheric and Solar-Terrestrial Physics*, *70*(11-12), 1482–1496. doi: 10.1016/j.jastp.2008.04.020

Brum, C. G. M., Rodrigues, F. D. S., Santos, P. T. D., Matta, A. C., Aponte, N., Gonzalez, S. A., & Robles, E. (2011). A modeling study of fof2 and hmf2 parameters measured by the Arecibo incoherent scatter radar and comparison with IRI model predictions for solar cycles 21, 22, and 23. *Journal of Geophysical Research: Space Physics*, *116*(A3). doi: 10.1029/2010ja015727

Burns, A. G., Solomon, S. C., Wang, W., Qian, L., Zhang, Y., & Paxton, L. J. (2012). Daytime climatology of ionospheric NmF2 and hmf2 from COSMIC data. *Journal of Geophysical Research: Space Physics*, *117*(A9). doi: 10.1029/2012ja017529

Chamberlin, P. C., Woods, T. N., & Eparvier, F. G. (2007, July). Flare Irradiance Spectral Model (FISM): Daily component algorithms and results. *Space Weather*, *5*(7), S07005. doi: 10.1029/2007SW000316

Chamberlin, P. C., Woods, T. N., & Eparvier, F. G. (2008). Flare Irradiance Spectral Model (FISM): Flare component algorithms and results. *Space Weather*, *6*(5). doi: 10.1029/2007sw000372

Chen, Z., Zhang, S.-R., Coster, A. J., & Fang, G. (2015). EOF analysis and modeling of GPS TEC climatology over North America. *Journal of Geophysical Research: Space Physics*, *120*(4), 3118–3129. doi: 10.1002/2014ja020837

Cherniak, I., Zakharenkova, I., Krankowski, A., & Shagimuratov, I. (2012). Plasmaspheric electron content derived from GPS TEC and FORMOSAT-3/COSMIC measurements: Solar minimum condition. *Advances in Space Research*, *50*(4), 427–440. doi: 10.1016/j.asr.2012.04.002

Emmert, J. T., Picone, J. M., & Meier, R. R. (2008). Thermospheric global average density trends, 1967–2007, derived from orbits of 5000 near-earth objects. *Geophysical Research Letters*, *35*(5). doi: 10.1029/2007gl032809

Feng, J. F., Han, B., Zhao, Z., & Wang, Z. (2019). A new global total electron content empirical model. *Remote Sensing*, *11*, 706. doi: 10.3390/rs11060706

Fuller-Rowell, T. J. (1998). The "thermospheric spoon": A mechanism for the semiannual density variation. *Journal of Geophysical Research: Space Physics*, *103*(A3), 3951–3956. doi: 10.1029/97ja03335

Gu, S.-Y., Ruan, H., Yang, C.-Y., Gan, Q., Dou, X., & Wang, N. (2018). The morphology of the 6-day wave in both the neutral atmosphere and f region ionosphere under solar minimum conditions. *Journal of Geophysical Research: Space Physics*, *123*(5), 4232–4240. doi: 10.1029/2018ja025302

Gulyaeva, T., Arikan, F., Sezen, U., & Poustovalova, L. (2018). Eight proxy indices of solar activity for the international reference ionosphere and plasmasphere model. *Journal of Atmospheric and Solar-Terrestrial Physics*, *172*, 122–128. doi: 10.1016/j.jastp.2018.03.025

Habarulema, J. B., Mckinnell, L.-A., & Opperman, B. D. (2010). TEC measurements and modelling over Southern Africa during magnetic storms; a compar-

ative analysis. *Journal of Atmospheric and Solar-Terrestrial Physics*, *72*(5-6), 509–520. doi: 10.1016/j.jastp.2010.01.012

Habarulema, J. B., Mckinnell, L.-A., & Opperman, B. D. L. (2011). Regional GPS TEC modeling; Attempted spatial and temporal extrapolation of TEC using neural networks. *Journal of Geophysical Research: Space Physics*, *116*(A4). doi: 10.1029/2010ja016269

He, C., Yang, Y., Carter, B., Kerr, E., Wu, S., Deleflie, F., ... et al. (2018). Review and comparison of empirical thermospheric mass density models. *Progress in Aerospace Sciences*, *103*, 31–51. doi: 10.1016/j.paerosci.2018.10.003

Heath, D. F., & Schlesinger, B. M. (1986). The Mg 280-nm doublet as a monitor of changes in solar ultraviolet irradiance. *Journal of Geophysical Research*, *91*(D8), 8672–8682. doi: 10.1029/jd091id08p08672

Huang, Z., & Yuan, H. (2014). Ionospheric single-station TEC short-term forecast using RBF neural network. *Radio Science*, *49*(4), 283–292. doi: 10.1002/2013rs005247

ISO14222. (2013). *Iso 14222: Space environment (natural and artificial) – earth upper atmosphere.* Retrieved from `https://www.iso.org/standard/54507.html`

ISO16457. (2014). *Iso 16457: Space systems – space environment (natural and artificial) – the earth's ionosphere model: international reference ionosphere (iri) model and extension to the plasmasphere.* Retrieved from `https://www.iso.org/standard/61556.html`

Jacchia, L. G. (1959). Solar effects on the acceleration of artificial satellites. *SAO Special Report*, *29*.

Jakowski, N., Mayer, C., Hoque, M. M., & Wilken, V. (2011). Total electron content models and their use in ionosphere monitoring. *Radio Science*, *46*(6). doi: 10.1029/2010rs004620

Jones, M., Emmert, J. T., Drob, D. P., Picone, J. M., & Meier, R. R. (2018). Origins of the thermosphere-ionosphere semiannual oscillation: Reformulating the "thermospheric spoon" mechanism. *Journal of Geophysical Research: Space Physics*, *123*(1), 931–954. doi: 10.1002/2017ja024861

Kim, D.-S., & Dong-Ku, S. (2011). *A standardization technique to reduce the problem of multicollinearity in polynomial regression analysis.* Retrieved from `http://stat.fi/isi99/proceedings/arkisto/varasto/kim_0574.pdf`

Komjathy, A., Sparks, L., Wilson, B. D., & Mannucci, A. J. (2005). Automated daily processing of more than 1000 ground-based gps receivers for studying intense ionospheric storms. *Radio Science*, *40*(6). doi: 10.1029/2005rs003279

Kumar, S. (2016). Performance of IRI-2012 model during a deep solar minimum and a maximum year over global equatorial regions. *Journal of Geophysical Research: Space Physics*, *121*(6), 5664–5674. doi: 10.1002/2015ja022269

Kumar, S., Tan, E. L., & Murti, D. S. (2015). Impacts of solar activity on performance of the IRI-2012 model predictions from low to mid latitudes. *Earth, Planets and Space*, *67*(1). doi: 10.1186/s40623-015-0205-3

Lean, J. L. (2019). One- to 10-day forecasts of ionospheric total electron content using a statistical model. *Space Weather*, *17*(2), 313–338. doi: 10.1029/2018sw002077

Lean, J. L., Meier, R. R., Picone, J. M., Sassi, F., Emmert, J. T., & Richards, P. G. (2016). Ionospheric total electron content: Spatial patterns of variability. *Journal of Geophysical Research: Space Physics*, *121*(10), 10,367-10,402.

Lean, J. L., Woods, T. N., Eparvier, F. G., Meier, R. R., Strickland, D. J., Correira, J. T., & Evans, J. S. (2011). Solar extreme ultraviolet irradiance: Present, past, and future. *Journal of Geophysical Research: Space Physics*, *116*(A1). doi: 10.1029/2010ja015901

Lei, J., Liu, L., Wan, W., & Zhang, S.-R. (2005). Variations of electron density based on long-term incoherent scatter radar and ionosonde measurements over

Millstone Hill. *Radio Science*, *40*(2). doi: 10.1029/2004rs003106

Li, S., Li, L., & Peng, J. (2016). Variability of Ionospheric TEC and the Performance of the IRI-2012 Model at the BJFS Station, China. *Acta Geophysica*, *64*(5), 1970–1987. doi: 10.1515/acgeo-2016-0075

Liu, J., Chen, R., An, J., Wang, Z., & Hyyppa, J. (2014). Spherical cap harmonic analysis of the Arctic ionospheric TEC for one solar cycle. *Journal of Geophysical Research: Space Physics*, *119*(1), 601–619. doi: 10.1002/2013ja019501

Liu, J., Liu, L., Zhao, B., Wan, W., & Chen, Y. (2012). Empirical modeling of ionospheric F2 layer critical frequency over Wakkanai under geomagnetic quiet and disturbed conditions. *Science China Technological Sciences*, *55*(5), 1169–1177. doi: 10.1007/s11431-012-4801-1

Liu, L., Wan, W., Ning, B., Pirog, O. M., & Kurkin, V. I. (2006). Solar activity variations of the ionospheric peak electron density. *Journal of Geophysical Research*, *111*(A8). doi: 10.1029/2006ja011598

Liu, L., Yao, Y., Kong, J., & Shan, L. (2018). Plasmaspheric Electron Content Inferred from Residuals between GNSS-Derived and TOPEX/JASON Vertical TEC Data. *Remote Sensing*, *10*(4), 621. doi: 10.3390/rs10040621

Lu, G., Goncharenko, L. P., Richmond, A., Roble, R., & Aponte, N. (2008). A dayside ionospheric positive storm phase driven by neutral winds. *Journal of Geophysical Research: Space Physics*, *113*(A8).

Machol, J., Snow, M., Woodraska, D., Woods, T., Viereck, R., & Coddington, O. (2019). An improved lyman-alpha composite. *Earth and Space Science*, *6*(12), 2263–2272. doi: 10.1029/2019ea000648

Mannucci, A. J., Wilson, B. D., Yuan, D. N., Ho, C. H., Lindqwister, U. J., & Runge, T. F. (1998). A global mapping technique for gps-derived ionospheric total electron content measurements. *Radio Science*, *33*(3), 565–582. doi: 10.1029/97rs02707

Mao, T., Wan, W., Yue, X., Sun, L., Zhao, B., & Guo, J. (2008). An empirical orthogonal function model of total electron content over China. *Radio Science*, *43*(2). doi: 10.1029/2007rs003629

Mao, T., Wan, W.-X., & Liu, L.-B. (2005). An EOF based empirical model of TEC over Wuhan. *Chinese Journal of Geophysics*, *48*(4), 827–834. doi: 10.1002/cjg2.720

Maruyama, T. (2010). Solar proxies pertaining to empirical ionospheric total electron content models. *Journal of Geophysical Research: Space Physics*, *115*(A4). doi: 10.1029/2009ja014890

Maruyama, T. (2011). Modified solar flux index for upper atmospheric applications. *Journal of Geophysical Research: Space Physics*, *116*(A8). doi: 10.1029/2010ja016322

Mendillo, M. (2006). Storms in the ionosphere: Patterns and processes for total electron content. *Reviews of Geophysics*, *44*(4). doi: 10.1029/2005rg000193

Mukhtarov, P., Andonov, B., & Pancheva, D. (2013a). Global empirical model of TEC response to geomagnetic activity. *Journal of Geophysical Research: Space Physics*, *118*(10), 6666–6685. doi: 10.1002/jgra.50576

Mukhtarov, P., Pancheva, D., Andonov, B., & Pashova, L. (2013b). Global TEC maps based on GNSS data: 1. Empirical background TEC model. *Journal of Geophysical Research: Space Physics*, *118*(7), 4594–4608. doi: 10.1002/jgra.50413

Nava, B., Coïsson, P., & Radicella, S. (2008). A new version of the NeQuick ionosphere electron density model. *Journal of Atmospheric and Solar-Terrestrial Physics*, *70*(15), 1856–1862. doi: 10.1016/j.jastp.2008.01.015

Prölss, G. W. (1995). Ionospheric f-region storms. *Handbook of atmospheric electrodynamics*, *2*, 195–248.

Qin, Y., Gu, S., Dou, X., Gong, Y., Chen, G., Zhang, S., & Wu, Q. (2019). Climatology of the Quasi-6-Day Wave in the Mesopause Region and Its Modulations

on Total Electron Content During 2003–2017. *Journal of Geophysical Research: Space Physics*, *124*(1), 573–583. doi: 10.1029/2018ja025981

Richards, P. G. (2001). Seasonal and solar cycle variations of the ionospheric peak electron density: Comparison of measurement and models. *Journal of Geophysical Research: Space Physics*, *106*(A7), 12803–12819. doi: 10.1029/2000ja000365

Richards, P. G., Fennelly, J. A., & Torr, D. G. (1994). EUVAC: A solar EUV Flux Model for aeronomic calculations. *Journal of Geophysical Research*, *99*(A5), 8981. doi: 10.1029/94ja00518

Rideout, W., & Coster, A. (2006). Automated gps processing for global total electron content data. *GPS Solutions*, *10*(3), 219–228. doi: 10.1007/s10291-006-0029-5

Rishbeth, H., Müller-Wodarg, I. C. F., Zou, L., Fuller-Rowell, T. J., Millward, G. H., Moffett, R. J., & et al. (2000). Annual and semiannual variations in the ionospheric F2-layer: II. Physical discussion. *Annales Geophysicae*, *18*(8), 945–956. doi: 10.1007/s00585-000-0945-6

Scherliess, L., Tsagouri, I., Yizengaw, E., Bruinsma, S., Shim, J. S., Coster, A., & Retterer, J. M. (2019). The international community coordinated modeling center space weather modeling capabilities assessment: Overview of ionosphere/thermosphere activities. *Space Weather*, *17*(4), 527–538. doi: 10.1029/2018sw002036

Schonfeld, S. J., White, S. M., Henney, C. J., Hock-Mysliwiec, R. A., & Mcateer, R. T. J. (2019). The Slowly Varying Corona. II. The Components of F 10.7 and Their Use in EUV Proxies. *The Astrophysical Journal*, *884*(2), 141. doi: 10.3847/1538-4357/ab3af9

Schunk, R. W., & Nagy, A. F. (2009). *Ionospheres: physics, plasma physics, and chemistry* (2nd ed.). Cambridge Univ. Press.

Shim, J. S., Jee, G., & Scherliess, L. (2017a). Climatology of plasmaspheric total electron content obtained from Jason 1 satellite. *Journal of Geophysical Research: Space Physics*, *122*(2), 1611–1623. doi: 10.1002/2016ja023444

Shim, J. S., Kuznetsova, M., Rastätter, L., Bilitza, D., Butala, M., Codrescu, M., ... et al. (2012). CEDAR Electrodynamics Thermosphere Ionosphere (ETI) challenge for systematic assessment of ionosphere/thermosphere models: Electron density, neutral density, NmF2, and hmF2 using space based observations. *Space Weather*, *10*(10). doi: 10.1029/2012sw000851

Shim, J. S., Kuznetsova, M., Rastätter, L., Hesse, M., Bilitza, D., Butala, M., & et al. (2011). CEDAR Electrodynamics Thermosphere Ionosphere (ETI) Challenge for systematic assessment of ionosphere/thermosphere models: NmF2, hmF2, and vertical drift using ground-based observations. *Space Weather*, *9*(12). doi: 10.1029/2011sw000727

Shim, J. S., Rastätter, L., Kuznetsova, M., Bilitza, D., Codrescu, M., Coster, A. J., ... et al. (2017b). CEDAR-GEM challenge for systematic assessment of ionosphere/thermosphere models in predicting TEC during the 2006 December storm event. *Space Weather*, *15*(10), 1238–1256. doi: 10.1002/2017sw001649

Shim, J. S., Tsagouri, I., Goncharenko, L., Rastaetter, L., Kuznetsova, M., Bilitza, D., ... et al. (2018). Validation of ionospheric specifications during geomagnetic storms: TEC and foF2 during the 2013 March storm event. *Space Weather*, *16*(11), 1686–1701. doi: 10.1029/2018sw002034

Tariku, Y. A. (2016). The study of variability of TEC over mid-latitude American regions during the ascending phase of solar cycle 24 (2009–2011). *Advances in Space Research*, *58*(4), 598–608. doi: 10.1016/j.asr.2016.05.012

Tariku, Y. A. (2019). Mid latitude ionospheric TEC modeling and the IRI model validation during the recent high solar activity (2013–2015). *Advances in Space Research*, *63*(12), 4025–4038. doi: 10.1016/j.asr.2019.03.010

Themens, D. R., Jayachandran, P. T., Galkin, I., & Hall, C. (2017). The Empirical

Canadian High Arctic Ionospheric Model (E-CHAIM): NmF2 and hmF2. *Journal of Geophysical Research: Space Physics*, *122*(8), 9015–9031. doi: 10.1002/2017ja024398

Thomas, E., Baker, J., Ruohoniemi, J., Coster, A., & Zhang, S.-R. (2016). The geomagnetic storm time response of gps total electron content in the north american sector. *Journal of Geophysical Research: Space Physics*, *121*(2), 1744–1759.

Tobiska, W., & Bouwer, S. (2005). Solar flare evolution model for operational users. In J. Goodman (Ed.), *2005 ionospheric effects symposium* (p. 76–76). JMG Associates.

Tobiska, W. K. (2002). E10.7 use for global atmospheric density forecasting in 2001. *AIAA/AAS Astrodynamics Specialist Conference and Exhibit*. doi: 10.2514/6.2002-4892

Tobiska, W. K., Bouwer, S. D., & Bowman, B. R. (2008). The development of new solar indices for use in thermospheric density modeling. *Journal of Atmospheric and Solar-Terrestrial Physics*, *70*(5), 803–819. doi: 10.1016/j.jastp.2007.11.001

Vergados, P., Komjathy, A., Runge, T. F., Butala, M. D., & Mannucci, A. J. (2016). Characterization of the impact of glonass observables on receiver bias estimation for ionospheric studies. *Radio Science*, *51*(7), 1010–1021. doi: 10.1002/2015rs005831

Viereck, R., Puga, L., Mcmullin, D., Judge, D., Weber, M., & Tobiska, W. K. (2001). The Mg II index: A proxy for solar EUV. *Geophysical Research Letters*, *28*(7), 1343–1346. doi: 10.1029/2000gl012551

Vierinen, J., Coster, A. J., Rideout, W. C., Erickson, P. J., & Norberg, J. (2016). Statistical framework for estimating GNSS bias. *Atmospheric Measurement Techniques*, *9*(3), 1303–1312. doi: 10.5194/amt-9-1303-2016

Wieman, S., Didkovsky, L., & Judge, D. (2014). Resolving differences in absolute irradiance measurements between the soho/celias/sem and the sdo/eve. In *Coronal magnetometry* (pp. 285–303). Springer.

Wood, B. E., Lean, J. L., Mcdonald, S. E., & Wang, Y.-M. (2016). Comparative ionospheric impacts and solar origins of nine strong geomagnetic storms in 2010-2015. *Journal of Geophysical Research: Space Physics*, *121*(6), 4938–4965. doi: 10.1002/2015ja021953

Woods, T., Bailey, S., Eparvier, F., Lawrence, G., Lean, J., Mcclintock, B., & et al. (2000). TIMED solar EUV experiment. *Physics and Chemistry of the Earth, Part C: Solar, Terrestrial & Planetary Science*, *25*(5-6), 393–396. doi: 10.1016/s1464-1917(00)00040-4

Woods, T. N. (2005). Solar EUV Experiment (SEE): Mission overview and first results. *Journal of Geophysical Research*, *110*(A1). doi: 10.1029/2004ja010765

Yamazaki, Y., Stolle, C., Matzka, J., & Alken, P. (2018). Quasi-6-day wave modulation of the equatorial electrojet. *Journal of Geophysical Research: Space Physics*, *123*(5), 4094–4109. doi: 10.1029/2018ja025365

Yizengaw, E., Moldwin, M., Galvan, D., Iijima, B., Komjathy, A., & Mannucci, A. (2008). Global plasmaspheric TEC and its relative contribution to GPS TEC. *Journal of Atmospheric and Solar-Terrestrial Physics*, *70*(11-12), 1541–1548. doi: 10.1016/j.jastp.2008.04.022

Zakharenkova, I., Cherniak, I., Krankowski, A., & Shagimuratov, I. (2015). Vertical tec representation by IRI 2012 and IRI Plas models for European midlatitudes. *Advances in Space Research*, *55*(8), 2070–2076. doi: 10.1016/j.asr.2014.07.027

Zhang, S.-R., Holt, J. M., Erickson, P. J., & Goncharenko, L. P. (2015, May). Day-to-day variability and solar preconditioning of thermospheric temperature over Millstone Hill. *Journal of Geophysical Research: Space Physics*, *120*(5), 3913–3927.

Zhang, S.-R., Holt, J. M., van Eyken, A. P., McCready, M., Amory-Mazaudier, C.,

Fukao, S., & Sulzer, M. P. (2005). Ionospheric local model and climatology from long-term databases of multiple incoherent scatter radars. *Geophyical Research Letters*, *32*(20), 9481.